

Article

Compact Ammonia/Water Absorption Chiller of Different Cycle Configurations: Parametric Analysis Based on Heat Transfer Performance

Xuan Tao ^{1,2}, Dhinesh Thanganadar ¹ and Kumar Patchigolla ^{1,*} ¹ School of Water, Energy and Environment (SWEE), Cranfield University, Cranfield MK43 0AL, UK² Cryogenics Center, Zhejiang University City College, Hangzhou 310015, China

* Correspondence: k.patchigolla@cranfield.ac.uk

Abstract: Ammonia/water absorption chillers are driven by low-grade heat and cover wide refrigeration temperatures. This paper analyses single-stage ammonia/water absorption chillers. A numerical model was developed based on the heat exchanger performance. The model captures variational heat exchanger performances and describes the actual cycle with varying boundary conditions. The detrimental effects of refrigerant impurity were analysed quantitatively under different operating conditions. The model was validated with experimental data. A basic cycle and three advanced cycles were analysed for sub-zero refrigeration by comparing the thermodynamic performances. A compression-assisted cycle extended the activation temperature from 80 to 60 °C. At the heat source of 120 °C, when a counter-current desorber or bypassed rich solution was used, the COP increased from 0.51 to 0.58 or 0.57, respectively. The operating parameters included the heat source temperatures, heat sink temperatures, the mass flow rates and mass concentrations of rich solutions. Higher heat source temperatures increase cooling capacity. The increase was around 20 kW for the basic cycle of sub-zero refrigeration. There is an optimum heat source temperature maximising the COP. Higher heat source temperatures increased the refrigerant mass flow rate and reduced the mass concentration. The mass concentration can decrease from 0.999 to 0.960.

Keywords: ammonia/water; cycle configurations; temperature glide; heat source temperature; heat transfer model; plate heat exchanger; absorption cooling; solar refrigeration



Citation: Tao, X.; Thanganadar, D.; Patchigolla, K. Compact Ammonia/Water Absorption Chiller of Different Cycle Configurations: Parametric Analysis Based on Heat Transfer Performance. *Energies* **2022**, *15*, 6511. <https://doi.org/10.3390/en15186511>

Academic Editor: Fabio Polonara

Received: 13 August 2022

Accepted: 28 August 2022

Published: 6 September 2022

Publisher's Note: MDPI stays neutral with regard to jurisdictional claims in published maps and institutional affiliations.



Copyright: © 2022 by the authors. Licensee MDPI, Basel, Switzerland. This article is an open access article distributed under the terms and conditions of the Creative Commons Attribution (CC BY) license (<https://creativecommons.org/licenses/by/4.0/>).

1. Introduction

The challenge of global warming will increasingly change future energy transfer and conversion processes, with renewable energy being a key feature of a low/zero carbon future. The refrigeration industry has a large potential for carbon mitigation by upgrading to renewable and sustainable approaches. In 2016, the electricity consumption of space cooling was 2000 TWh worldwide, which accounted for nearly 18.5% of that in buildings. The electricity consumption of space cooling was 3% of global primary energy use [1]. This electricity consumption was dramatically reduced by replacing it with low-grade heat.

Solar refrigeration is one of the most promising options [2,3]. Solar energy harvest technology has been rapidly developed, and mature technology is available in low temperature ranges (<240 °C) [4]. Evacuated tube collectors and compound parabolic collectors provide fluid with temperatures of around 100 °C, which meets the heating requirement of absorption refrigeration [4].

Absorption refrigeration utilises low-grade heat. The primary working pairs are ammonia/water and water/lithium bromide. Water/lithium bromide systems have been widely used because refrigerant purification is eased, leading to a high Coefficient of Performance (COP). However, the refrigeration temperature is limited by the freezing of water and must be kept above 0 °C. Water/lithium bromide systems are not suitable for high environment temperatures because of crystallisation [5].

An ammonia/water system meets the sub-zero refrigeration demand and is applicable to high environment temperatures. The driving temperature is 70–120 °C for single-stage [6,7]. The main drawback is the low COP due to the ammonia rectification between the desorber and condenser. The developments of ammonia-based absorption systems are focused on COP improvement and application extension. The optimisation approaches have been comprehensively discussed in open literature, which mainly include adding components to the basic cycles, rearrangement of cycle configurations, using novel working pairs and adding surfactant to the working fluids [6–9]. The cycle configurations were investigated to improve the thermal efficiency and compactness:

- Internal heat recovery: the heat of rectification, absorption and condensation was reused to preheat the strong solution instead of dissipating it into the environment. The temperature of the strong solution was lifted before entering the desorber so that the net heating load was reduced. The generator absorber heat exchange (GAX) cycle made use of the temperature overlap between the desorber and absorber. The overlapped heat was transferred from the absorber to desorber. The GAX component was introduced in two-stage cycles and is located in either the high-pressure circuit or low-pressure circuit. With multi-effect cycles, the condensation heat was recovered solely or was combined with absorption heat to generate refrigerant vapour [5,10]. Solution recirculation was used when the desorber and absorber had large temperature glides. The desorber was divided into two parts. The rich solution was heated internally in the first part by the vapour leaving the desorber, and was then externally heated in the second part. Similarly, the absorber was composed of the internally cooled part and externally cooled part. Another configuration was the stream separation. The rich solution leaving the absorber was separated into two streams, which flowed into the solution heat exchanger and rectifier, respectively [11]. Internal heat recovery was restrained by the pinch point temperature difference. The optimal cycle configuration depends on the operating conditions and needed to be investigated individually [12].
- Size reduction: small-scale ammonia/water systems were developed so that the chillers were mobile or met the residential requirement. The heat and mass transfer devices were microscale and are non-commercial, thus new design methods were required [13,14]. A counter-current desorber purified the refrigerant vapour and reduced the rectifier load, which facilitates compact units. The accurate prediction of transport processes helped to optimise the system design [15,16].
- Compression-assisted absorption: a booster compressor was integrated in the absorption cycle, and the system operated at three pressure levels. The compressor had two locations. A low-pressure compressor was located between the evaporator and absorber, which increased the absorption pressure or reduced the evaporation pressure. A high-pressure compressor was between the desorber and condenser, lowering the desorption pressure or increasing the condensation pressure. The compressor promoted the vapour generation and augmented the cooling capacity [17,18].

Ammonia/water absorption cycles have been widely investigated with experiments and numerical models [19,20]. The experimental research has mostly measured the overall cycle performance but has not captured operational issues in depth. For example, the water content of ammonia refrigerant deteriorates the performance. But the refrigerant mass concentration is seldom measured, which is important to quantify the performance deterioration. Numerical models have the potential to investigate the operation details, which include pinch point analysis, heat exchanger efficiency method and conductance (*UA*) model. Pinch point analysis is used to design the cycle configurations, but cannot predict the performance of heat exchangers [12,21]. When pinch point or heat exchanger efficiency are used for analysis, the working fluids are usually assumed as saturated states at the outlet of heat exchangers, which do not reflect the actual operation [22,23].

The *UA* model is close to the actual cycle [5]. In simplified models, the *UA* value is assumed to be constant, which is convenient for the preliminary design but is less accurate for off-design conditions [13]. Solar driven absorption cycles cope with a varying heat

source. Thus, the chiller should perform favourably, not only in optimum conditions, but also in a wide range of operating conditions. The mass flow rates and mass concentrations of the working fluids are functions of boundary conditions, which change the UA value during off-design operation. The resulting variation of heat exchanger performance has not been fully investigated when integrated into a cycle. The heat transfer processes of absorption cycle include absorption, desorption, evaporation, condensation and single-phase heat transfer. The heat exchanger performance determines the operating parameters of absorption cycles. For example, the rich solution must be subcooled at the absorber outlet. The mass flow rates and mass concentrations of the rich solution are limited by the heat transfer performance of the absorber. Thus, a detailed analysis of heat exchanger performance is needed, which helps to locate the bottleneck of the thermodynamic performance.

In ammonia/water system, water is volatile and vaporises with the refrigerant. The importance of refrigerant purification has been widely recognised, while the discussion is mostly qualitative [5,24,25]. Fernández-Seara et al. [26] and Fernández-Seara and Sieres [27] built a model of distillation columns and compared different configurations. Ammonia concentration in the vapour refrigerant directly affects the operating pressures and system COP, which was quantified with a simplified system model. Osman and Guo [25] assumed that the rectifier has a constant efficiency. In other numerical models, the refrigerant is assumed to be pure ammonia [23], or the rectification process is not considered [22].

The water content in the ammonia refrigerant has a detrimental effect on cycle performance, bringing about a temperature glide during the phase change process at the condenser and evaporator [5]. The saturation temperature of ammonia/water is higher than pure ammonia. For condensation, the temperature difference between the refrigerant and secondary fluid is increased, which promotes the heat transfer. But the temperature difference during evaporation is reduced. Moreover, water content in the ammonia refrigerant produces mass transfer resistance, which decreases the Heat Transfer Coefficients (HTCs) of condensation [28]. Although the overall performances of ammonia/water absorption chillers have been widely reported, the influence of refrigerant impurity has not been evaluated quantitatively. In this paper, the variation of refrigerant impurity is quantified as a function of operating conditions, which explains the COP deterioration because of temperature glide and HTCs reduction.

In this study, a numerical model was developed for single-stage ammonia/water absorption chillers. The system was composed of Plate Heat Exchangers (PHEs), making the overall structure compact [3,7]. The off-design cycle model integrated detailed heat exchanger models. The variational heat exchanger performances were analysed with changing boundary conditions. The model was validated with experimental results. In the case studies of sub-zero refrigeration temperature, different cycle configurations were compared. The advantages of advanced cycles relative to a basic cycle depend on heat source temperatures. The mass flow rates and mass concentrations of the rich solution had major influences on the cooling capacity and COP, which were limited by the heat transfer performance of the absorber. The above-zero refrigeration temperature was also discussed. The heat sink temperature is the secondary fluid temperature of the absorber and condenser. A lower heat sink temperature improves the temperature driving force of the absorber so that the ammonia mass concentration can be increased.

2. Methodology

Figure 1 is the flow diagram of the basic cycle. The rich solution was heated by the heat source fluid at the desorber, where vapour of high ammonia concentration was generated. The vapour and poor solution flowed co-currently and left the desorber at the outlet (4 and 7). The vapour was partly condensed and was purified at the rectifier, where the heat was recovered by the rich solution. The reflux from the rectifier was mixed with the poor solution at the inlet of the Solution Heat Exchanger (SHE) (4 and 8). The vapour refrigerant was cooled by the heat sink fluid of the condenser. At the Refrigerant Heat Exchanger (RHE), the refrigerant was subcooled by the cold stream exiting the evaporator. Since the

refrigerant was not pure ammonia, the evaporation was restrained by the temperature glide. The refrigerant left the evaporator as a two-phase fluid or superheated vapour, which was dependent on the refrigerant mass concentration. The remaining cooling capacity was recovered at the RHE. The refrigerant and poor solution were mixed when entering the absorber (14 and 6). At the absorber outlet, the rich solution was subcooled (1). The rich solution recovered heat from the refrigerant at the rectifier and from the poor solution at the SHE.

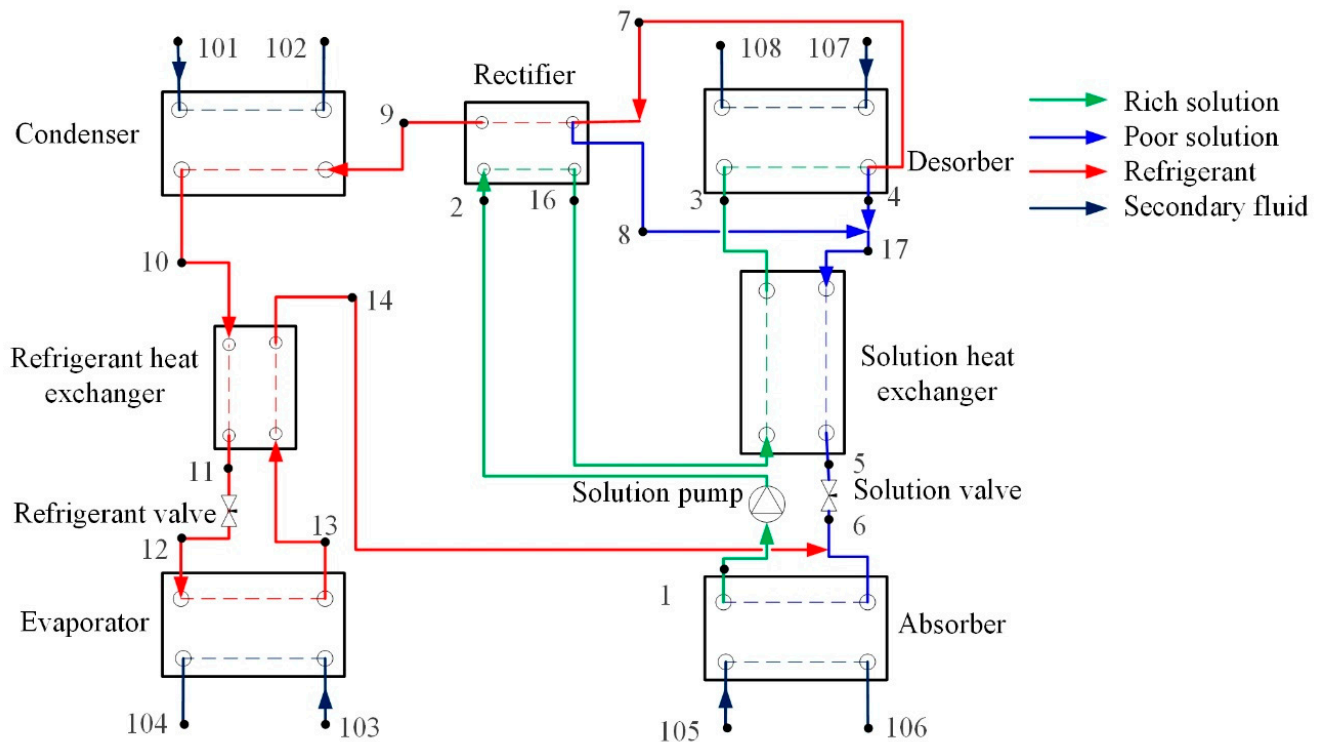


Figure 1. Flow diagram of the basic single-stage ammonia/water absorption cycle with internally cooled rectifier and refrigerant heat exchanger.

It was possible to improve the thermodynamic efficiency of the basic cycle by integrating a compressor, optimising refrigerant purification and augmenting internal heat recovery. In this paper, advanced cycles are discussed, and different configurations are compared, including a compression-assisted cycle, a cycle with counter-current desorber and a cycle with bypassed rich solution.

Figure 2 shows the flow diagram of the compression-assisted cycle. The refrigerant leaving the RHE flows into a compressor, and the pressure is raised. The system operates at three pressure levels. The evaporator and cold side of the RHE have low pressure. The absorber is middle pressure. The other heat exchangers are on the high pressure side. Consequently, the mass concentration of the rich solution can be increased at the absorber.

In Figure 3, the solution and refrigerant vapour flow counter-currently at the desorber. The vapour leaving the desorber is in direct contact with the rich solution (4 and 7), and the vapour mass concentration is increased. The reflux from the rectifier flows back to the desorber inlet and is mixed with the rich solution (8 and 3).

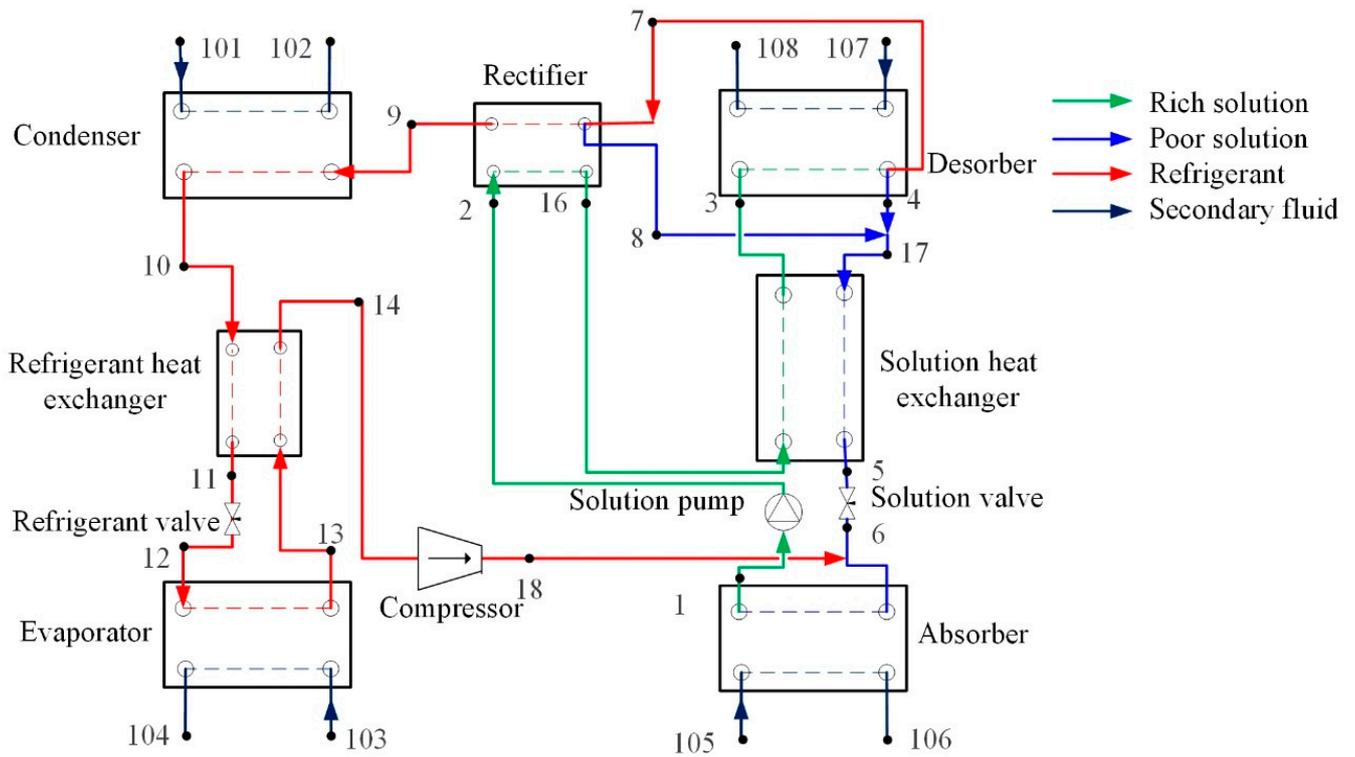


Figure 2. Flow diagram of compression-assisted ammonia/water absorption cycle.

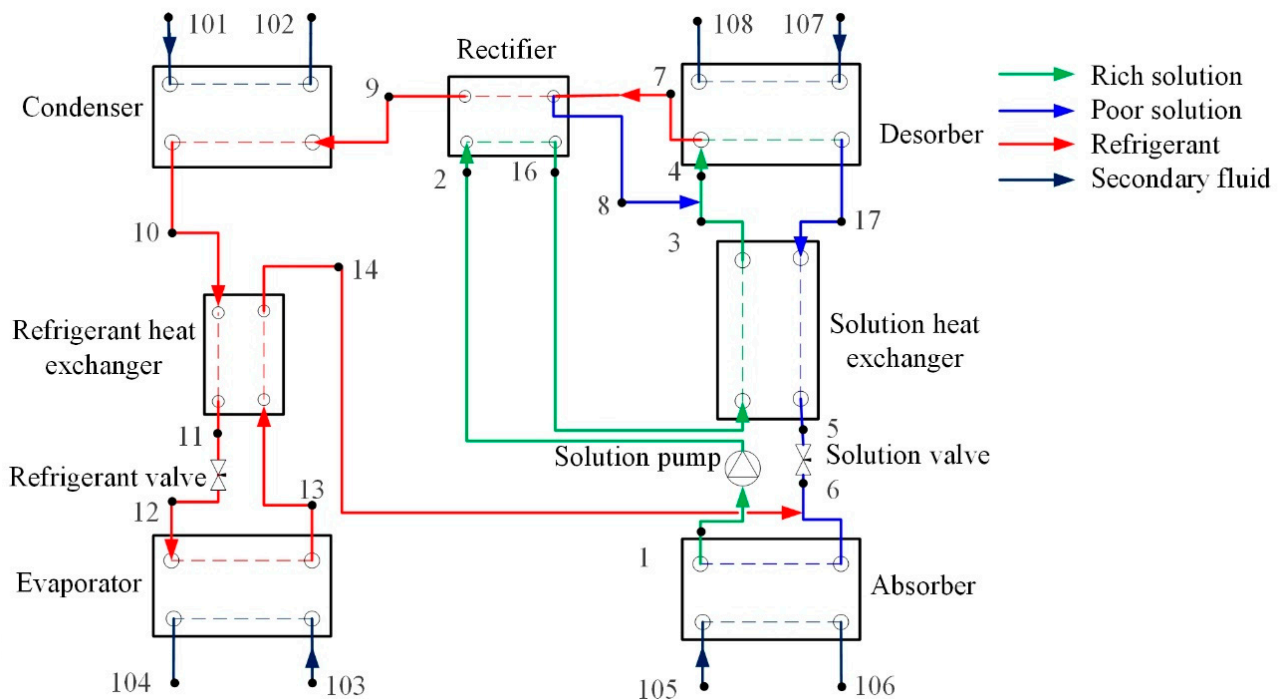


Figure 3. Flow diagram of ammonia/water absorption cycle with counter-current desorber.

At the SHE of the basic cycle, the rich solution had a larger mass flow rate than the poor solution. The pinch point temperature difference was at the cold end. In Figure 4, a part of the rich solution is bypassed into the rectifier after the solution pump. The rest of the rich solution enters the SHE. The two parts of the rich solution are fully preheated and are mixed before flowing into the desorber (3 and 16).

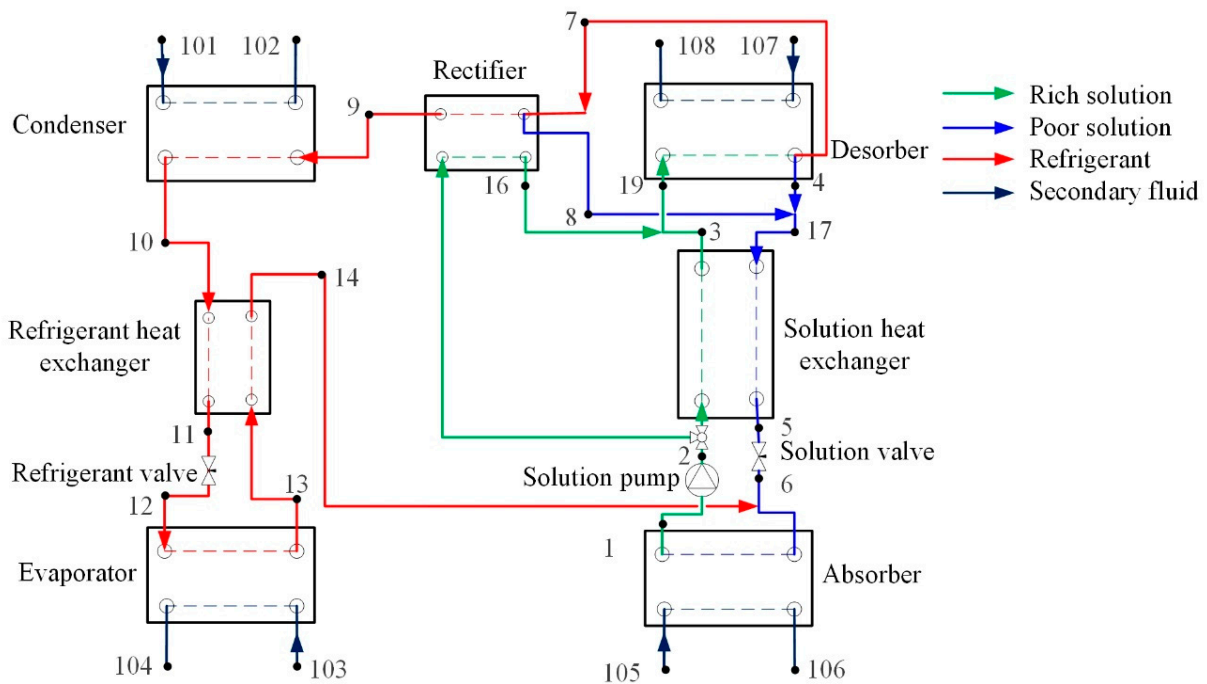


Figure 4. Flow diagram of ammonia/water absorption cycle with bypassed rich solution.

2.1. Integrated Cycle and Heat Exchanger Models

The cycle was modelled by solving thermodynamic energy and mass balance equations and heat transfer equations. Figure 5 is the schematic of the model structure. The input parameters are the mass flow rate and mass concentration of the rich solution, as well as the boundary conditions of the secondary fluids.

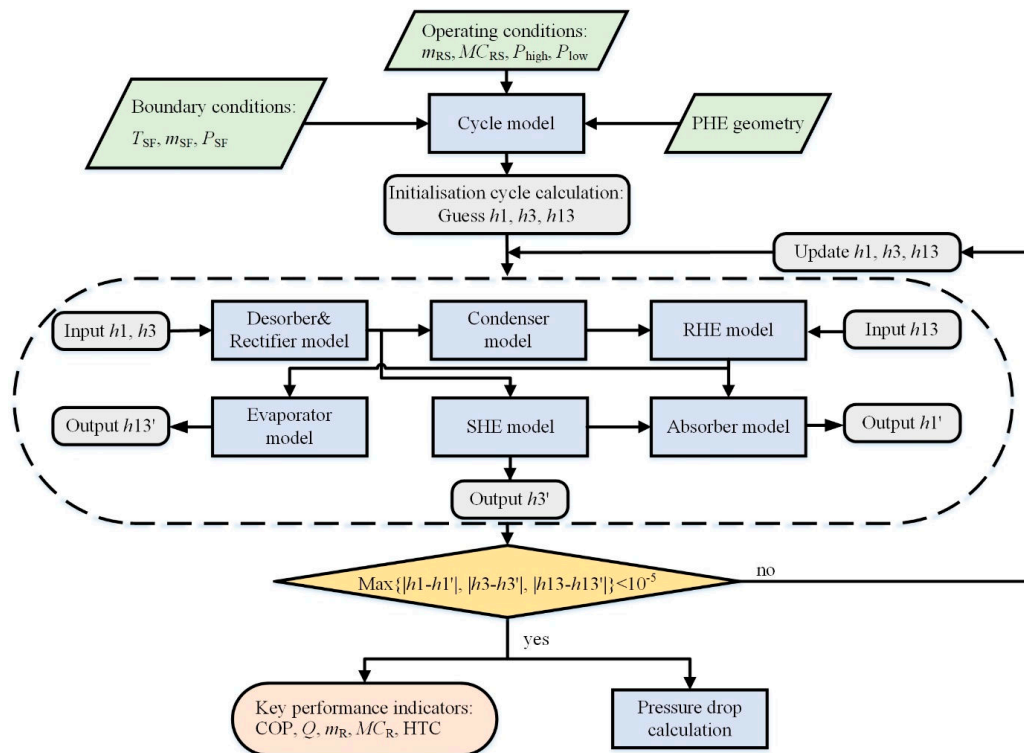


Figure 5. Simulation platform of the integrated cycle model and heat exchanger models.

The operating pressures were dependent on the heat source and heat sink temperatures. The desorber had the same pressures as the condenser, which were both on the high-pressure side. The absorber and evaporator had the same pressure and were on the low-pressure side. For given boundary temperatures, the condensation pressure determines the temperature driving force of the desorber and condenser. Higher condensation pressure reduced the temperature driving force of the desorber but raised the temperature driving force of the condenser. Thus, a small amount of refrigerant was generated at the desorber, which was likely to be subcooled at the condenser. On the other hand, lower condensation pressure promotes the generation of the refrigerant at the desorber. But the temperature driving force of the condenser was small, and the refrigerant could not be fully condensed. According to experimental work, the condensation pressure is a function of heat source and heat sink temperatures [13,19]. Higher heat source or heat sink temperatures increase the condensation pressure. More refrigerant is generated at higher heat source temperatures, which increases the heat load of the condenser. The condensation pressure increases to transfer the heat load. When the heat sink temperature increases, the condensation pressure is increased to maintain the temperature driving force. In this study, the condensation pressure was determined so that the refrigerant was completely condensed at the condenser.

Similarly, the temperature driving forces of the evaporator and absorber are functions of the evaporation pressure. The evaporation pressure is restrained by the absorber. At low evaporation pressure, the absorber has a small temperature driving force, and the rich solution cannot be subcooled. Vapour accumulates at the outlet, which increases the evaporation pressure. When the evaporation pressure is high, the temperature driving force of the evaporator is small. The cooling capacity is reduced. In accordance with experimental work, the evaporation pressure increases with higher heat source and heat sink temperatures [13,20]. Higher heat source temperatures contribute to more refrigerant and increase the heat load of the absorber. Higher heat sink temperatures reduce the temperature driving force of the absorber. Consequently, the evaporation pressure is increased. In this study, the evaporation pressure was determined so that the rich solution was subcooled at the absorber outlet. In practice, liquid tanks should be installed at the outlets of the condenser and absorber to stabilise the operation, which do not affect the energy balance and are not shown in Figures 1–4.

Detailed heat exchanger models were integrated with the cycle model. PHEs were used as the desorber, condenser, evaporator, SHE and absorber. The HTCs were calculated with the geometric parameters of the PHEs. Referring to Figures 1–4, the enthalpies of the states 1, 3 and 13 (h_1 , h_3 and h_{13}) were initialised by the cycle model and then iterated. The states of the downstream points were calculated as functions of the heat exchanger performance. For example, the outlet conditions of the desorber were calculated with state 3, the heat transfer area of the desorber and secondary fluid. Enthalpy instead of temperature was used as the iteration parameter. Enthalpy changes smoothly from superheated vapour to subcooled liquid. The calculated values of h_1 , h_3 and h_{13} using the heat exchanger models were compared with the estimated values that resulted from the cycle model. The iteration is finished when the values agree. Otherwise, h_1 , h_3 and h_{13} are updated. The iteration was implemented using the Matlab `fsolve` algorithm [29]. The output parameters were the cycle COP, the heat loads of all the heat exchangers, the mass flow rate and mass concentration of the refrigerant, as well as the HTCs. The pressure drops in the heat exchangers were small and were neglected during the iteration. When the iteration was finished, the pressure drops were estimated separately.

2.2. Modelling Method

The model integrates thermodynamic mass and energy balance calculations and heat transfer prediction. It is based on the following assumptions:

- The operation of the cycle is steady state.
- The pressure drops of the working fluids in the heat exchangers do not affect the heat transfer performance. The absorber and evaporator have the same operating pressures

except for the compression-assisted cycle. The desorber, rectifier, condenser and SHE have identical operating pressures. The pressure drops are determined after the heat transfer calculation is converged.

- Higher heat source and heat sink temperatures increase the operating pressures, so that the refrigerant is completely condensed at the condenser and the rich solution is subcooled at the absorber outlet.
- Referring to Figures 1, 2 and 4, at the desorber and rectifier, states 4 and 8 are saturated liquid. States 7 and 9 are saturated vapour. State 7 is in equilibrium with state 4 ($T_7 = T_4$). T_7 and T_8 have a temperature difference of 10 K because of the mass transfer resistance ($T_7 = T_8 + 10$). This value is based on the investigation of small scale rectifiers [16,30]. Similarly, in the cycle of Figure 3, states 17 and 8 are saturated liquid. States 7 and 9 are saturated vapour. State 7 has the same temperature as state 4 ($T_7 = T_4$). T_7 and T_8 have a temperature difference of 10 K ($T_7 = T_8 + 10$).
- The working fluids and secondary fluids are uniformly distributed in the channels of the PHEs. The heat leakage to the environment is neglected.
- The expansion valves do not restrain the mass flow rate of working fluid. The expansion processes are isenthalpic.
- At the evaporator outlet, unevaporated liquid droplets are entrained by the vapour flow. No water is accumulated. In the following analysis, the ammonia refrigerant has more water content under larger mass flow rate, and the entrainment effects are stronger.

The thermodynamic model was derived from the mass, mass concentration and energy balances of the components. Equations (1)–(3) are the control equations. Equation (4) calculates the cycle COP. It is the ratio of the cooling capacity to the heating capacity and consumed power. For the compression-assisted cycle, the power consumption included the pump power and compressor power. For the other cycles, only the pump power was involved. The pump power was much smaller than the heating capacity. The efficiency of the solution pump was assumed to be 50% [31]. Since the pump power was less than 2% of the heating capacity, the pump efficiency had a little effect on the cycle COP.

$$\sum m_{in} = \sum m_{out} \quad (1)$$

$$\sum m_{in} MC_{in} = \sum m_{out} MC_{out} \quad (2)$$

$$Q = \sum m_{out} h_{out} - \sum m_{in} h_{in} \quad (3)$$

$$COP = \frac{Q_{Eva}}{Q_{Des} + W_{SP} + W_{Com}} \quad (4)$$

The counter current heat exchanger models used the log mean temperature difference (LMTD) method. In Equation (5), the actual heat transfer areas of PHEs consider the area enlargement of corrugated plates [32]. The HTC of the working fluids and secondary fluids are functions of the operating conditions. The working fluids have temperature glides, which is quantified by the LMTD in Equation (6).

$$Q = U \cdot A \cdot LMTD = \frac{A}{\frac{1}{\alpha_{WF}} + d_p/\lambda + \frac{1}{\alpha_{SF}}} LMTD \quad (5)$$

$$LMTD = \frac{(T_{hot,in} - T_{cold,out}) - (T_{hot,out} - T_{cold,in})}{\ln \frac{T_{hot,in} - T_{cold,out}}{T_{hot,out} - T_{cold,in}}} \quad (6)$$

The solution circulation ratio is the mass flow rate ratio of rich solution to refrigerant, which is calculated in Equation (7). It measures the amount of refrigerant generated per unit rich solution. The solution circulation ratio also indicates the imbalance between the rich and poor solutions at the SHE.

$$f = \frac{m_1}{m_9} \quad (7)$$

In absorption cycles, the heat transfer processes include the desorption and absorption of solutions, the condensation and evaporation of refrigerant, as well as single-phase heat transfer. Applicable correlations were selected for PHEs and were implemented in the model. The details of the correlations were provided in the Appendix A.

The desorption heat transfer of ammonia/water was estimated by the correlation of Taboas et al. [33,34]. The desorption process had large mass flow rates and low vapour qualities. The nucleate boiling process was degraded by the mass transfer resistance. Convective boiling enhanced the heat transfer. Cerezo et al. [35] proposed a heat transfer correlation for water-cooled bubble absorbers. The liquid and vapour flowed upward. The heat transfer was enhanced by lower solution mass concentration, lower cooling water temperature and higher operating pressure. The correlation of two-phase inlet was used in the present model.

Ammonia has a high thermal conductivity and a large two-phase density ratio, whose heat transfer of evaporation and condensation shows distinct characteristics from other refrigerants [36]. Khan et al. [37] developed a heat transfer correlation for ammonia evaporation. The heat transfer is dominated by convective boiling in the narrow channels. Tao and Infante Ferreira [36] proposed a heat transfer correlation of ammonia condensation based on flow patterns. Convective condensation prevails for large liquid mass fluxes, while gravity-controlled condensation becomes noticeable for small liquid mass fluxes. The ammonia refrigerant contained a small amount of water. The temperature glide of evaporation reduced the temperature driving force and the heat transfer deteriorated. Although the temperature glide of condensation enlarged the temperature driving force, the HTC was degraded because of mass transfer resistance. The mixture degradation of condensation was quantified using the Silver [38] and Bell and Ghaly [39] method.

At SHE, the heat transfer took place between single-phase working fluids. At the desorber, condenser, evaporator and absorber, the secondary fluids are single-phase flows. Single-phase heat transfer was predicted using the correlation of Martin [40].

The rectifier has a large temperature driving force. The UA value is small. In this paper, the rectifier was assumed to have a constant UA value. At the RHE, the cold fluid was the refrigerant from the evaporator and contained water, which has a sharp temperature change. The heat transfer of the RHE was calculated with a pinch point temperature difference of 5 K.

The pressure drops of the working fluids and secondary fluids in the heat exchangers were calculated after the cycle iteration was converged. The working fluid is in two-phase flow at the desorber, condenser, evaporator and absorber, which shows separated flow characteristics [34,37,41]. The two-phase pressure drop was calculated with a separated flow correlation [36]. Both pure ammonia and ammonia/water have a large two-phase density ratio. The mass transfer resistance of the mixture had a minor influence on pressure drops. The pressure drop correlation of pure ammonia is applicable for ammonia/water [28]. The working fluid was single-phase flow at the SHE. The secondary fluids also flowed in single-phase. The pressure drop was predicted using the correlation of Martin [40].

The thermodynamic properties of ammonia/water were calculated using Refprop, such as enthalpy, temperature, pressure, density and mass concentration [42]. The transport properties of the mixture used Conde including thermal conductivity and dynamic viscosity [43]. The fluid properties of aqueous solutions were determined by Melinder [44].

3. Model Validation

The numerical model was validated with two sets of experimental data, whose refrigeration temperatures were above-zero and sub-zero, respectively. The experimental setup performed well in design conditions, and the corresponding data were chosen for validation. In off-design conditions, the performance of the absorption system deteriorated as the expansion valve had limited flow passage capability [19,20,45]. The experimental setup had a slightly different configuration from that in Figure 1. For example, the experimental setup had no RHE. The numerical model was adjusted to reflect the actual configuration.

3.1. Above-Zero Refrigeration

Le Lostec et al. [19] experimentally studied a single-stage absorption chiller. An adiabatic rectifier was installed between the desorber and condenser. The rich solution flowed into the top of the rectifier. The chiller had a high COP at design conditions when the refrigeration temperature at the evaporator inlet was close to 10 °C. When the refrigeration temperature decreased, the refrigerant was not completely evaporated, and the COP was degraded. The refrigerant mass flow rate could not be effectively reduced by the expansion valve. In this section, the model was compared with six cases with refrigeration temperatures close to 10 °C. Table 1 lists the operating parameters.

Table 1. Operating parameters of the experimental data [19].

Parameter	COP	P_{high}	P_{low}	Des		Eva		Con		Abs	
				T_{SF}	m_{SF}	T_{SF}	m_{SF}	T_{SF}	m_{SF}	T_{SF}	m_{SF}
Unit	-	kPa	kPa	°C	kg s ⁻¹						
Case1	0.60	1300	530	86	0.52	19	0.82	22	0.33	22	0.56
Case2	0.54	1400	630	85	0.24	19	0.42	22	0.21	22	0.36
Case3	0.47	1400	660	85	0.51	20	0.83	22	0.33	22	0.56
Case4	0.60	1250	560	76	0.51	19	0.82	22	0.32	22	0.56
Case5	0.61	1260	610	75	0.23	19	0.42	22	0.21	22	0.37
Case6	0.58	1250	620	76	0.50	19	0.83	22	0.33	22	0.56

In Figure 6, the predicted values are compared with the experimental data for the six cases with different heat source temperatures, operating pressures and mass flow rates. The input parameters were the high and low operating pressures, the inlet temperatures and the mass flow rates of the secondary fluids. The output parameters were the heat loads of the heat exchangers.

Generally, the experimental heat loads of the heat exchangers were accurately predicted by the numerical model. The deviations of the desorber and evaporator were smaller than 4% and 6%, respectively. The predicted heat loads of the condenser were about 30% larger than the experimental values. During the experiments, to promote cooling, the condenser and absorber were not insulated [19]. The condenser had a high temperature, and the heat loss to the environment was significant. The temperature of the absorber was close to the environment, and the heat loss was minor. The experimental data of SHE was not measured. The predicted values are presented, which are comparable to that of the desorber.

As shown in Table 1, the heat sink temperatures of the condenser and absorber were constant. The heat source temperatures of Cases 1–3 were 85–86 °C. In Figure 6a, Case 1 has lower operating pressures than Cases 2–3, which increases the temperature driving force at the desorber and evaporator. Large cooling capacity was achieved. The predicted COP was 0.62. In Case 2 of Figure 6b, the mass flow rates of the secondary fluids are the smallest, which restricts the heat loads. The cooling capacity was small. The COP was predicted to be 0.54. Case 3 had high operating pressures and large mass flow rates of the secondary fluids. Low COP was achieved and was 0.49. Cases 4–6 had lower heat source temperatures that are 75–76 °C. The corresponding heat loads of the heat exchangers were smaller than those of Cases 1–3. The mass flow rates of the secondary fluids were almost the same for Cases 1 and 4. The desorber heat load of Case 4 was about 25% smaller than that of Case 1. The predicted COP of Cases 4–6 was 0.61, 0.58 and 0.60, respectively.

3.2. Sub-Zero Refrigeration

Jiménez-García and Rivera [20] built a single-stage absorption chiller with PHEs. The rectifier was externally cooled, and the heat was not recovered. The heat exchangers were oversized, and the pinch point temperature difference was close to zero. It was possible to upgrade the cooling capacity by increasing the mass flow rates. The refrigeration tempera-

ture at the evaporator inlet was below -10°C , whereas the corresponding secondary fluid had a higher temperature.

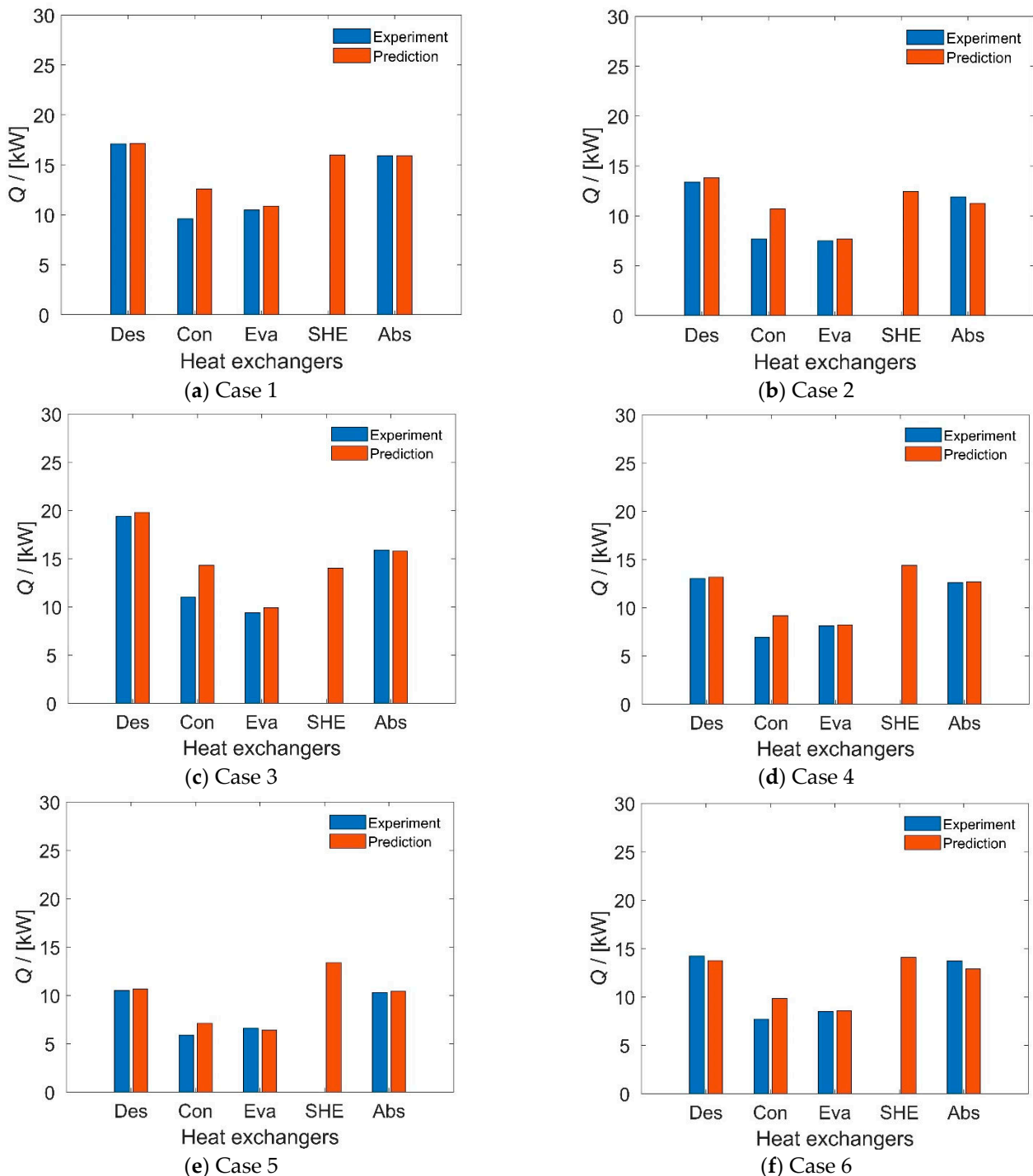


Figure 6. Comparison of the predicted heat loads through this study with the experimental data of Le Lostec et al. [19] for (a) Case 1, (b) Case 2, (c) Case 3, (d) Case 4, (e) Case 5, (f) Case 6.

The driving temperature was the inlet temperature of the secondary fluid at the desorber, while the heat sink temperatures were the inlet temperatures of the secondary fluids at the absorber and condenser. In this section, the model results are compared with the experimental data [20]. As shown in Table 2, six cases were compared. The mass flow rates and inlet temperatures of the secondary fluids are presented. In Cases 1–3, the heat

sink temperature of the condenser was 24 °C. The heat source temperature increased from 95 °C to 105 °C. Cases 4–6 had a condenser heat sink temperature of 28 °C. The mass flow rates of the secondary fluids were constant, which are shown in the notes of Table 2. The operating pressures were determined by the heat source temperature.

Table 2. Comparison of the numerical model results with the experimental data of Jiménez-García and Rivera [20].

Parameter	$T_{SE,Des}$	$T_{SE,Con}$	$T_{SE,Eva}$	$T_{SE,Abs}$	P_{high}	P_{low}	Q_{Eva}		m_R		COP	
							Exp.	Pre.	Exp.	Pre.	Exp.	Pre.
Unit	°C	°C	°C	°C	kPa	kPa	kW	kW	kg/s	kg/s	-	-
Case 1	95	24	20	22	1340	270	1.41	1.35	0.00105	0.00113	0.568	0.556
Case 2	100	24	20	22	1360	280	2.30	1.94	0.00170	0.00163	0.603	0.586
Case 3	105	24	20	22	1400	290	2.36	2.40	0.00177	0.00199	0.614	0.591
Case 4	95	28	20	22	1400	270	0.48	0.48	0.00038	0.00040	0.436	0.417
Case 5	100	28	20	22	1420	280	1.02	0.94	0.00076	0.00079	0.515	0.509
Case 6	105	28	20	22	1450	290	2.31	2.17	0.00173	0.00182	0.585	0.577
$m_{SE,Des} = 0.267 \text{ kg s}^{-1}$		$m_{SE,Eva} = 0.167 \text{ kg s}^{-1}$			$m_{SE,Abs} = 0.2 \text{ kg s}^{-1}$			$m_{SE,Con} = 0.2 \text{ kg s}^{-1}$				

In Table 2, the experimental values of cooling capacity, refrigerant mass flow rate and COP are compared with the prediction. The predicted cooling capacity coincides to a large extent with the experimental value. During the experiments, the flow passage capability of the expansion valve was limited [20]. The experimental mass flow rate of the refrigerant was restrained, which was slightly over-predicted by the numerical model. The heat exchangers had large areas, which resulted in the upper limit of COP. In the tested ranges, the experimental results were accurately predicted by the numerical model. The relative error of COP was smaller than 5%.

4. Results and Discussion

Two scenarios were analysed with the numerical model. One scenario was a freezer with sub-zero refrigeration temperatures. The other was above-zero refrigeration. Two types of PHEs were used in the absorption cycles. The geometrical parameters are listed in Table 3. Type 1 had long plates, whose length was twice that of type 2.

Table 3. Geometrical parameters of the PHE.

Type	L_p	W_p	A_{per}	d_h	β	ϕ	d_g	d_p	Λ_{wave}
	mm	mm	m ²	mm		-	mm	mm	mm
1	668	95	0.0730	2.99	63°	1.15	1.72	0.58	6.67
2	334	95	0.0365	2.99	63°	1.15	1.72	0.58	6.67

4.1. Sub-Zero Refrigeration

In this scenario, the refrigeration temperature was sub-zero. Four cycle configurations are discussed. Table 4 presents the input parameters of the secondary fluids. The hot water temperature generally increased from 80 °C to 120 °C, which is liquid under the high operating pressure. For the other secondary fluids, the inlet temperatures were kept constant. The evaporator used aqueous solution of ethanol with a mass concentration of 30%, which was antifreeze [44].

Table 4 also presents the types and channels of the heat exchangers. The desorber, SHE and absorber have PHEs of long plates (type 1). The working fluids were rich and poor solutions, which had large mass flow rates. The heat loads and heat transfer areas were large. The condenser and evaporator had PHEs of short plates (type 2). The rectifier had a small heat transfer rate, whose overall conductance (UA) was considered to be constant and was 0.1 kW K⁻¹.

Table 4. Input parameters of the heat exchangers and secondary fluids for sub-zero refrigeration.

Heat Exchangers	N ^a	A m ²	Secondary Fluid			
			Fluid	T _{in} °C	P _{in} kPa	m kg s ⁻¹
Des (Type 1)	13/12	1.751	Water	80–120	300	0.8
Con (Type 2)	11/10	0.730	Water	18	200	0.5
Eva (Type 2)	13/12	0.876	Aqueous solution of ethanol (30% MC)	0	200	0.8
SHE (Type 1)	9/8	1.168	-	-	-	-
Abs (Type 1)	13/12	1.751	Water	18	200	0.5

^a Channel number, the secondary fluid/rich solution has one more channel than the working fluid/poor solution.

4.1.1. Basic Cycle

The performance of basic cycle was analysed, as shown in Figure 1. The influence of heat source temperature was investigated for different mass flow rates and mass concentrations of the rich solution. The results are shown in Figure 7. According to the experiments, higher heat source temperatures increase both the high and low pressures [19,20]. The influence of the operating pressures is discussed in Section 2.1. In this analysis, the high and low pressures were determined by trial calculation. To ensure that the refrigerant was completely condensed at the condenser, the high pressures increased with the heat source temperature and were 860–1200 kPa. With increasing heat source temperatures, the low pressures increased from 160 to 240 kPa so that the rich solution was subcooled at the absorber outlet. The corresponding refrigerant temperature at the evaporator inlet was $-24\text{ }^{\circ}\text{C}$ to $-13\text{ }^{\circ}\text{C}$.

In Figure 7a,b, the trends of the cooling capacity and refrigerant mass flow rate are similar. The cooling capacity increases with higher heat source temperatures by generating more refrigerant. The activation temperature of the heat source was $80\text{ }^{\circ}\text{C}$. When the heat source temperature was lower than $80\text{ }^{\circ}\text{C}$, no refrigerant vapour was generated at the desorber. The rich solution of higher mass concentration promoted the generation of refrigerant and improved the cooling capacity. When the mass concentration increased from 0.387 to 0.406 at the mass flow rate of 0.1 kg s^{-1} , the cooling capacity was more than 10% larger. Larger mass flow rates of the rich solution increased the cooling capacity and refrigerant mass flow rates. With the mass flow rate increasing from 0.1 kg s^{-1} to 0.12 kg s^{-1} , the cooling capacity improved by about 10%.

Figure 7c presents the vapour mass concentrations at the outlet of the desorber and rectifier. The latter is the refrigerant mass concentration. Higher heat source temperatures reduced the mass concentrations. Water is the non-volatile content of ammonia/water mixture. At the desorber outlet, more water evaporated for higher heat source temperature. When the rich solution was 0.1 kg s^{-1} and 0.387, the rectifier improved the mass concentration from 0.931 to 0.998 for the heat source temperature of $100\text{ }^{\circ}\text{C}$. The reflux ratio at the hot end of the rectifier was 0.11. At the temperature of $120\text{ }^{\circ}\text{C}$, the mass concentration at the rectifier changed from 0.875 to 0.974. The reflux ratio was 0.17. The vapour quality at the evaporator outlet was dependent on the refrigerant mass concentration. For high mass concentration, the refrigerant was completely evaporated and was superheated vapour. The outlet vapour quality was decreased to about 0.8 when the refrigerant mass concentration was low at the heat source of $120\text{ }^{\circ}\text{C}$.

Figure 7d depicts the variation of COP. COP increases with heat source temperature at small values and then decreases. The maximum COP was achieved at $110\text{ }^{\circ}\text{C}$. For low heat source temperatures, the refrigerant mass concentration was high. Most refrigerant was evaporated to produce cooling capacity. It is beneficial to increase the heat source temperatures and to generate more refrigerant. However, at high heat source temperatures, the refrigerant mass concentration decreases because the generation of water vapour. It was not possible for the refrigerant to evaporate fully, which reduced the COP. Additionally, the SHE efficiency decreased for high heat source temperatures since the poor solution had a much smaller mass flow rate than the rich solution. The mass concentration and mass

flow rate of the rich solution directly affected the COP. The rich solution of higher mass concentration (0.406) had a higher COP. Larger mass flow rates of the rich solution reduced the COP as the heat exchanger effectiveness decreased.

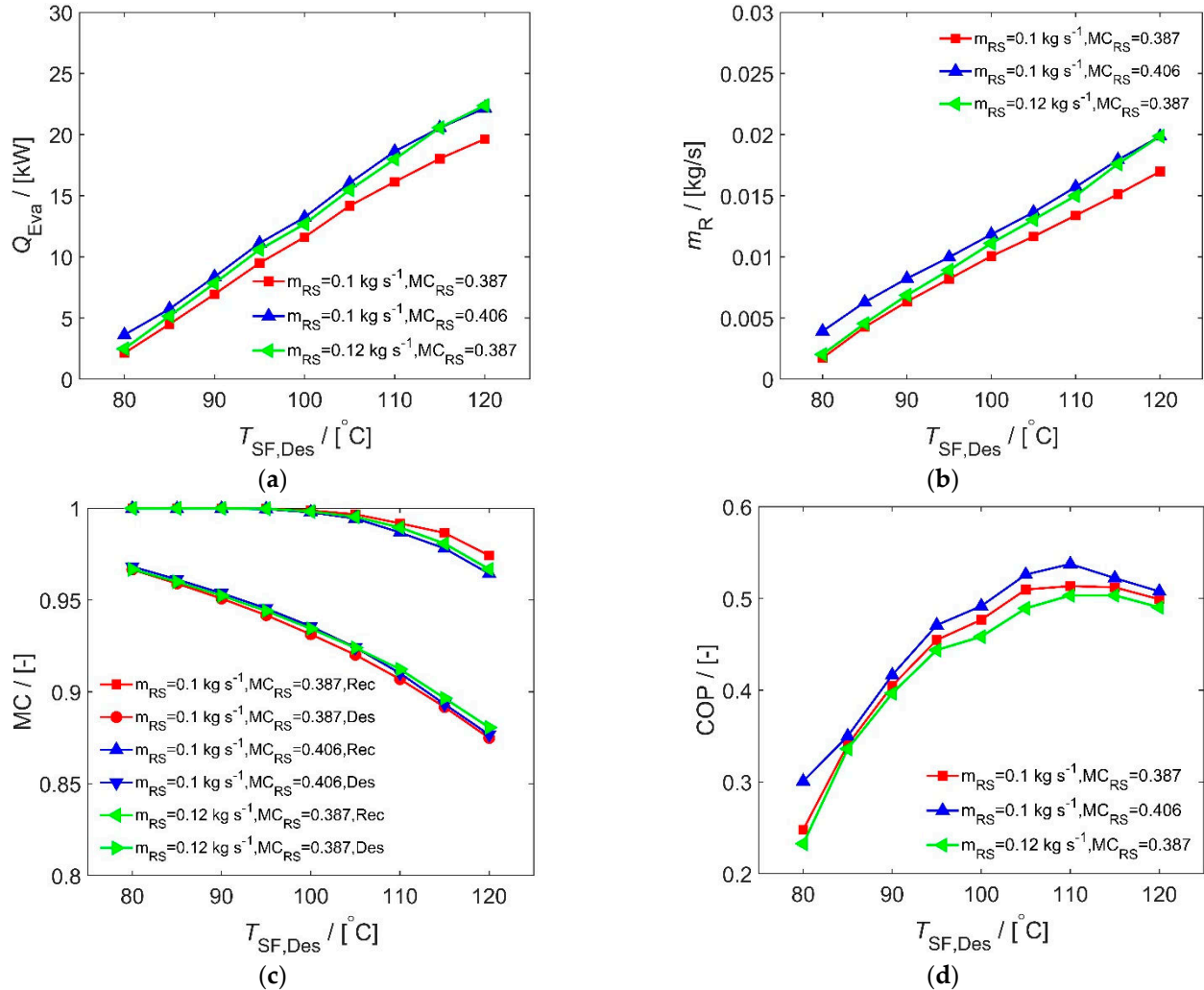


Figure 7. Performances of basic cycle as a function of heat source temperature, the mass flow rate and mass concentration of the rich solution. Cycle performances are (a) Cooling capacity, (b) Refrigerant mass flow rate, (c) Vapour mass concentration at the outlet of the desorber and rectifier, (d) COP.

When the rich solution has high mass concentrations, more refrigerant is generated at the desorber, achieving larger cooling capacity and higher COP. The rich solution with large mass flow rates has a larger cooling capacity and lower COP. The rich solution must be subcooled at the absorber outlet before flowing into the solution pump. The mass flow rates and mass concentrations are restrained by the heat transfer capacity of the absorber. In Figure 7, the rich solution is subcooled by 2–12 K.

The heat source fluid was provided by solar collectors. Higher fluid temperatures reduced the thermal efficiency of the collectors due to increased heat loss [4]. In Figure 7, the absorption cycle had an optimal heat source temperature that maximises the COP. For single-stage absorption cycles, high heat source temperatures increased the cooling capacity at the cost of the overall cycle efficiency.

Figure 8 gives the heat loads of all of the heat exchangers with varying heat source temperatures. The desorber heat loads increased sharply with heat source temperatures, and more refrigerant was generated. The condenser had a similar trend to the desorber. When the heat source temperature was low, such as 100 $^{\circ}C$, the heat load of the evaporator

was almost the same as that of the condenser. Most of the condensed refrigerant evaporated. When the heat source temperature was high, the evaporator had a smaller heat load than the condenser. The refrigerant had a lower mass concentration. During evaporation, the water content increased the saturation temperature at high vapour qualities, and thus the refrigerant left the evaporator with considerable amounts of liquid. The cooling capacity was lost at the evaporator and recovered at the RHE. The RHE heat loads increased noticeably with heat source temperatures. About 12% of the cooling capacity was recovered for the heat source of 120 °C. When the evaporator and condenser have equal heat loads, the heat loads of absorber are equivalent to those of the desorber. Otherwise, the non-evaporated water content flows into the absorber, and the absorber has smaller heat loads than the desorber. The SHE had steady heat loads. SHE transferred large amount of heat and reduced the heat input at the desorber. The rectifier had internal heat transfer, and the heat was recovered to preheat the rich solution. The heat loads of the rectifier accounted for 5%–18% of the heating capacity at the desorber.

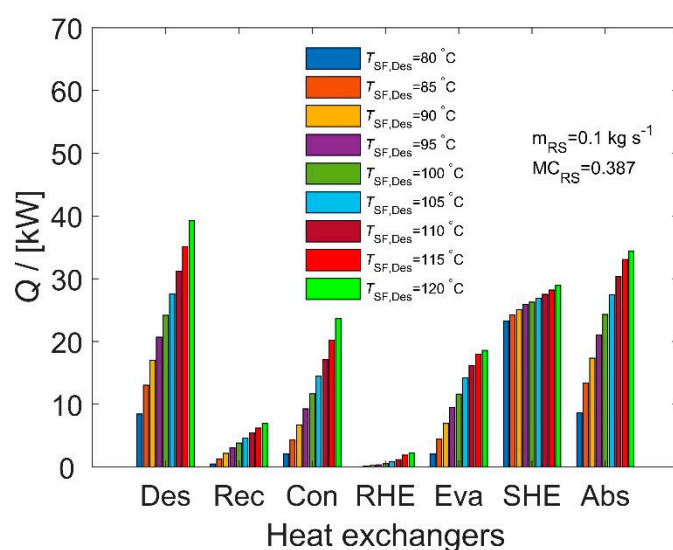


Figure 8. Heat exchanger loads as functions of heat source temperature for the rich solution of 0.1 kg s^{-1} and 0.387.

Figure 9 gives the HTC of the heat exchangers for the rich solutions of 0.1 kg s^{-1} and mass concentration 0.387. Figure 9a shows the overall HTCs. The condenser has the largest HTCs, while the SHE has the smallest HTCs. The overall HTCs are the combination of the HTCs on both sides, which are further presented in Figure 9b. At the SHE, the heat transfer of both sides was single-phase, and the HTCs were relatively small. For the other heat exchangers, phase change took place at the working fluid side. All the secondary fluids had large mass flow rates to enhance the heat transfer. When the secondary fluid was water, the HTCs were relatively large. The secondary fluid of the evaporator was an aqueous solution of ethanol, which was antifreeze and was appropriate for sub-zero refrigeration. Because of its large viscosity, the ethanol solution had small HTCs. The evaporator was required to have a large heat transfer area. The refrigerant had tiny amounts of water, which caused the deterioration of the heat transfer of condensation. The HTCs of high concentration ammonia/water were slightly smaller than the HTCs of pure ammonia and were larger than the HTCs at the desorber and absorber. With low mass concentration, the working fluid of desorption and absorption had a large mass transfer resistance. The HTCs of absorption were the lowest. In this analysis, the absorber had a pinch point temperature difference of 2.1–7.5 K.

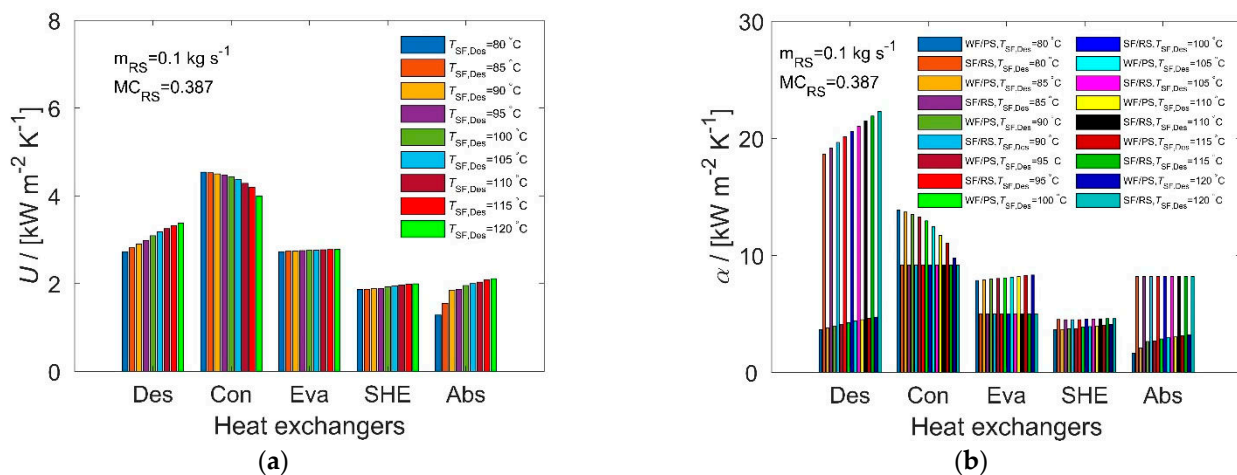


Figure 9. Overall HTCs (a) and two sides HTCs (b) of the heat exchangers for the rich solutions of 0.1 kg s^{-1} and mass concentration 0.387. For Des, Con, Eva and Abs, the two sides are working fluid (WF) and secondary fluid (SF). For SHE, the two sides are poor solution (PS) and rich solution (RS).

The pressure drops at the heat exchangers were neglected during the cycle calculation and were checked separately. Figure 7 covers several operating conditions. The pressure drops are functions of the mass flow rates and fluid properties. For the working fluids, the pressure drops of the desorber and absorber were smaller than 4 kPa and 26 kPa, respectively. The pressure drops of the condenser and evaporator were smaller than 1.2 kPa. The desorber and absorber had larger mass flow rates than the condenser and evaporator. These pressure drops were significantly smaller than the operating pressures. It was reasonable to neglect the pressure drop when predicting the heat exchanger performance. The pressure drop of all of the secondary fluids was smaller than 38 kPa. Since the secondary fluid was single-phase flow, it was acceptable to neglect the pressure drop during heat transfer calculation.

4.1.2. Compression-Assisted Cycle

Compression-assisted cycle is shown in Figure 2, and the performance is presented in Figure 10. When the pressure ratio is 1, the cycle is the same as the basic cycle. With the pressure ratio of 2, the mass concentration of the rich solution is increased to 0.486. The pressure ratio of 3 further increases the mass concentration to 0.536. With the increase of heat source temperature, the refrigerant leaving the evaporator changed from superheated vapour to two-phase fluids. The lowest vapour quality is 0.9. A screw compressor was chosen to cope with wet compression. The compressor isentropic efficiency was considered to be 70% [46]. The subcooling at the absorber outlet was 2–9 K.

As shown in Figure 10a,b, large pressure ratio and high mass concentration reduce the activation temperature of the heat source. Refrigerant vapour is generated at a lower heat source temperature. With the pressure ratio of 2 and 3, the activation temperature decreases to 65 °C and 60 °C, respectively. Large pressure ratio increases the cooling capacity and the refrigerant mass flow rate. When the heat source temperature is higher than 80 °C, the pressure ratio of 3 increases the cooling capacity by around 12 kW.

In Figure 10c, the large pressure ratio increased the vapour mass concentration at the desorber outlet. But the mass concentration improvement at the rectifier was smaller than that of the basic cycle. This was because the reflux ratio was small for a large pressure ratio and large refrigerant mass flow rate.

In Figure 10d, large pressure ratio increases COP, especially at low heat source temperatures. With the pressure ratio of 2 and 3, the maximum COP is achieved at 80 °C and 70 °C, respectively. Large pressure ratio results in a large refrigerant mass flow rate and low refrigerant mass concentration, so the maximum COP took place at lower heat

source temperature, where the SHE imbalance and refrigerant impurity caused smaller thermodynamic losses.

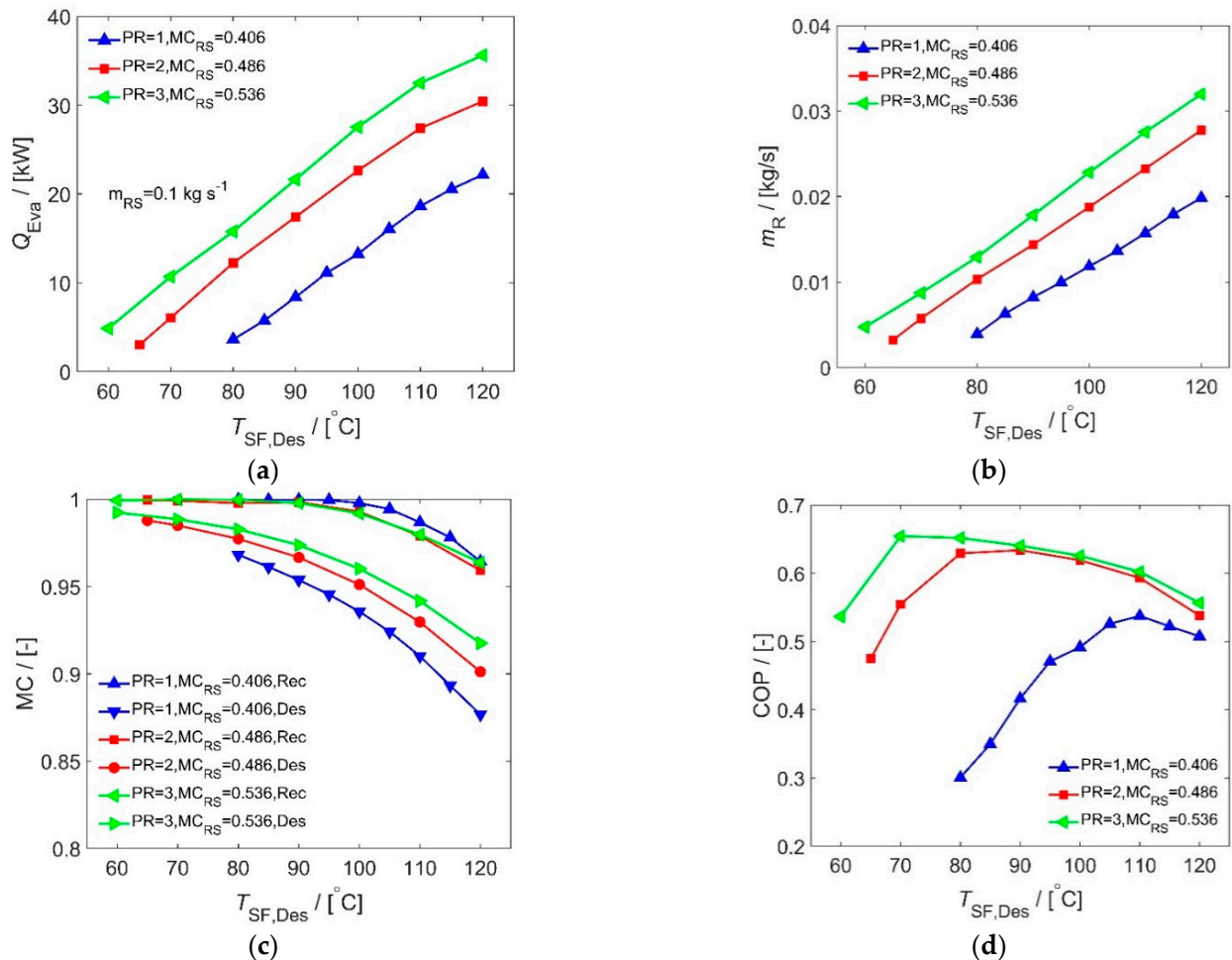


Figure 10. Performances of compression-assisted cycle as a function of heat source temperature and pressure ratio. Cycle performances are (a) Cooling capacity, (b) Refrigerant mass flow rate, (c) Vapour mass concentration at the outlet of the desorber and rectifier, (d) COP.

Figure 11 presents the heat loads of all the heat exchangers and the power consumption of the solution pump and compressor. Compared with the basic cycle in Figure 8, more heat was transferred between the working fluids and secondary fluids at the desorber, condenser, evaporator and absorber. This was attributed to the larger refrigerant mass flow rate. The SHE had smaller heat loads since the imbalance between the rich and poor solutions was more severe. The compressor power consumption increased noticeably with the heat source temperature, while the power consumption of the solution pump was negligible. At low heat source temperatures, compression-assisted cycle achieved major performance improvement with small compressor power consumption.

4.1.3. Cycle with Counter-Current Desorber

The flow diagram and performances of counter-current desorber are shown in Figures 3 and 12, respectively. The advanced cycle increased the vapour mass concentration at the desorber outlet, while the vapour mass flow rate stayed almost the same as the basic cycle. The cooling capacities of the advanced cycle only increased slightly. With counter-current desorber, the outlet vapour was in direct contact with the rich solution. Compared with co-current desorber, this vapour had a lower temperature and higher mass concentration, which is shown in Figure 12a. There was a great improvement of mass con-

centration at high heat source temperatures. According to Figure 12b, the counter-current desorber reduces the heat input. This was attributed to the fact that vapour of a higher ammonia mass concentration has smaller enthalpy. Less heat is required to generate the vapour. The heat input was reduced by 4.4 kW at 120 °C. As shown in Figure 12c, the advanced cycle had smaller heat loads for the rectifier, resulting from smaller temperature driving force. Small heat loads reduced the reflux ratio, and the purification effect was affected, which can be seen from Figure 12a. In Figure 12d, the counter-current desorber improved the COP, especially at high heat source temperatures. The COP was improved from 0.51 to 0.58 at 120 °C. The maximum COP took place at 115 °C. The evaporation of the water content was restrained, and the heat input was effectively used to generate ammonia vapour.

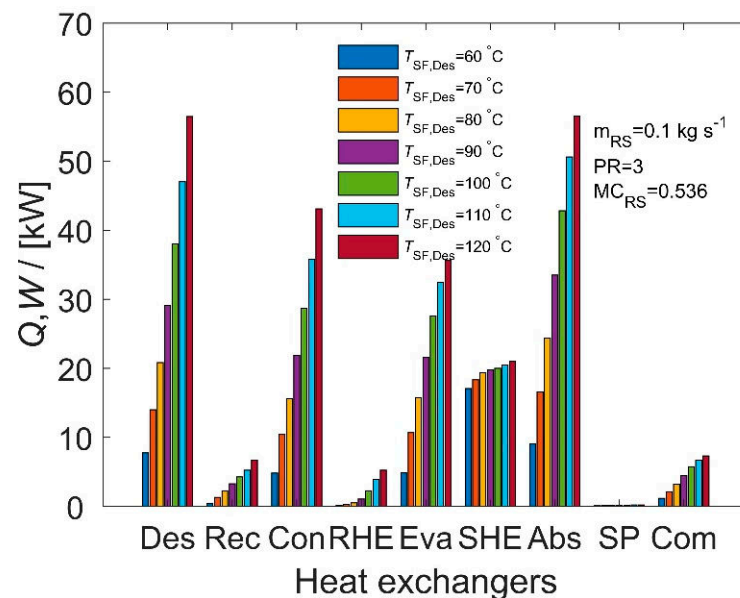


Figure 11. Heat exchanger loads and power consumption as functions of heat source temperature for the pressure ratio of 3.

4.1.4. Cycle with Bypassed Rich Solution

At the SHE of the basic cycle, the rich solution had a larger mass flow rate than the poor solution. Restrained by the pinch point temperature difference at the cold end, it was not possible to use the high temperature heat carried by the poor solution fully. To improve the internal heat recovery, an advanced cycle is shown in Figure 4. After the solution pump, the rich solution was divided into two streams. The main stream flowed into the SHE, while the other stream was bypassed and was heated at the rectifier. The main stream was controlled so as to have the same mass flow rate as the poor solution, so that the temperature difference between the two fluids was almost constant within the SHE and the rich solution was fully preheated.

In Figure 13, the performances of the cycle with bypassed rich solution are compared with those of basic cycle. The advanced cycle improves the COP noticeably at high heat source temperatures, while the improvement is minor at low heat source temperatures. The COP increased from 0.51 to 0.57 at 120 °C. As shown in Figure 13b, bypassed rich solution played an important role for a small solution circulation ratio, where the SHE showed a serious imbalance between the rich and poor solutions. The refrigerant mass flow rate of the advanced cycle was almost the same as that of the basic cycle.

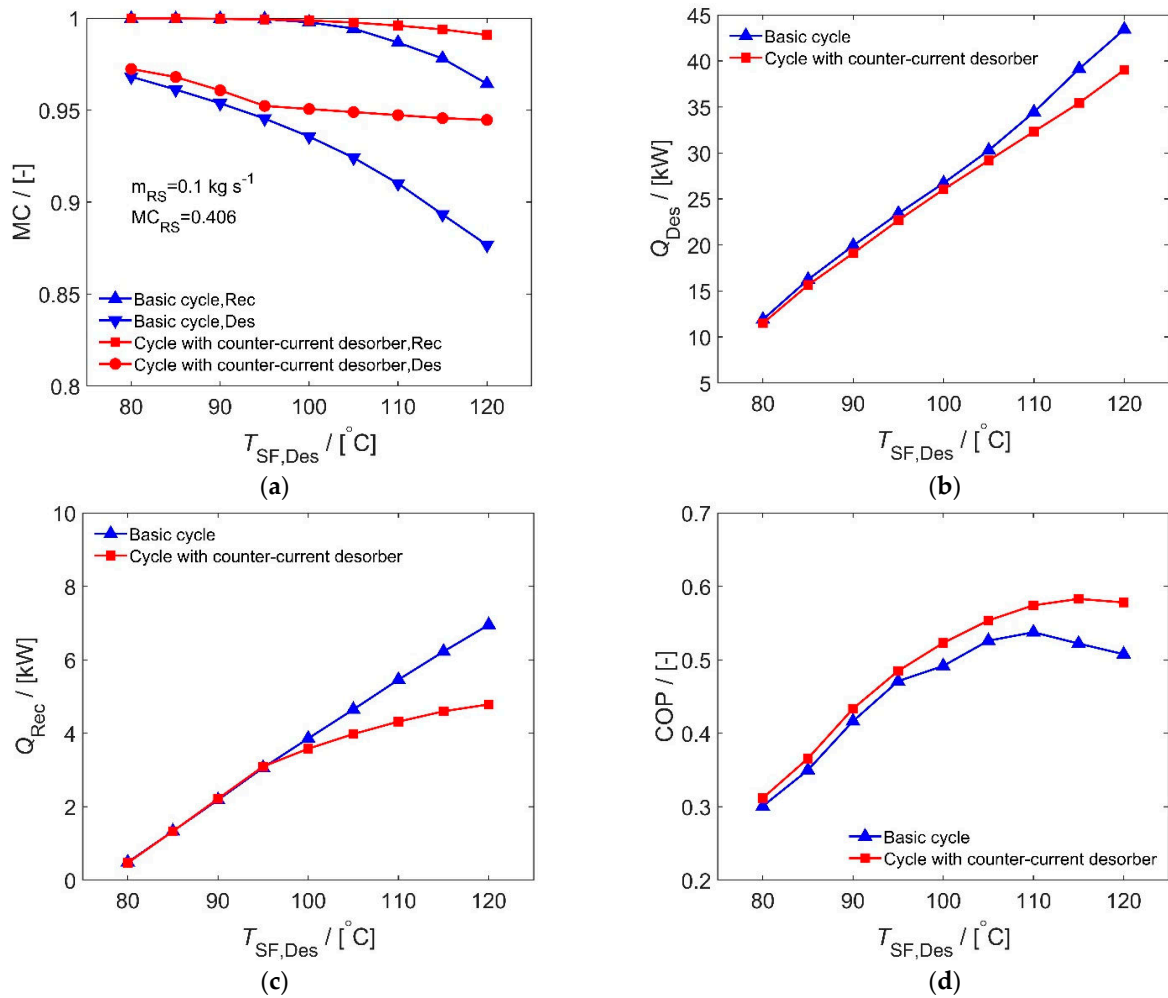


Figure 12. Performances of cycle with counter-current desorber and basic cycle as a function of heat source temperature. Cycle performances are (a) Vapour mass concentration at the outlet of the desorber and rectifier, (b) Heating capacity, (c) Heat loads of the rectifier, (d) COP.

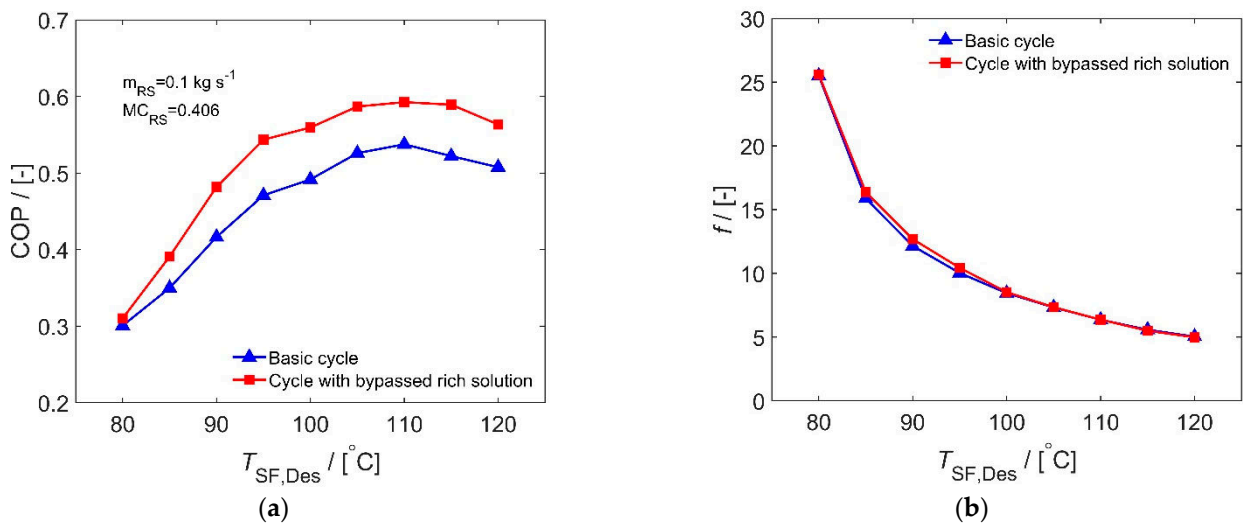


Figure 13. Performances of cycle with bypassed rich solution and basic cycle as a function of heat source temperature. Cycle performances are (a) COP, (b) Solution circulation ratio.

The influence of bypassed rich solution is further analysed in Figure 14. When the heat source temperature is 120 °C, the advanced cycle has a larger heat load for the SHE compared with the basic cycle, and the heat input at the desorber is reduced. Moreover, the poor solution was fully precooled at the SHE, and the heat load of the absorber decreased. The change of the cooling capacity was minor. At the heat source temperature of 80 °C, the bypassed rich solution had negligible effects. The SHE had a larger heat load than other heat exchangers. The heat input at the desorber was mostly used to increase the sensible heat of the solution, while only a small part was converted as the latent heat of the vapour.

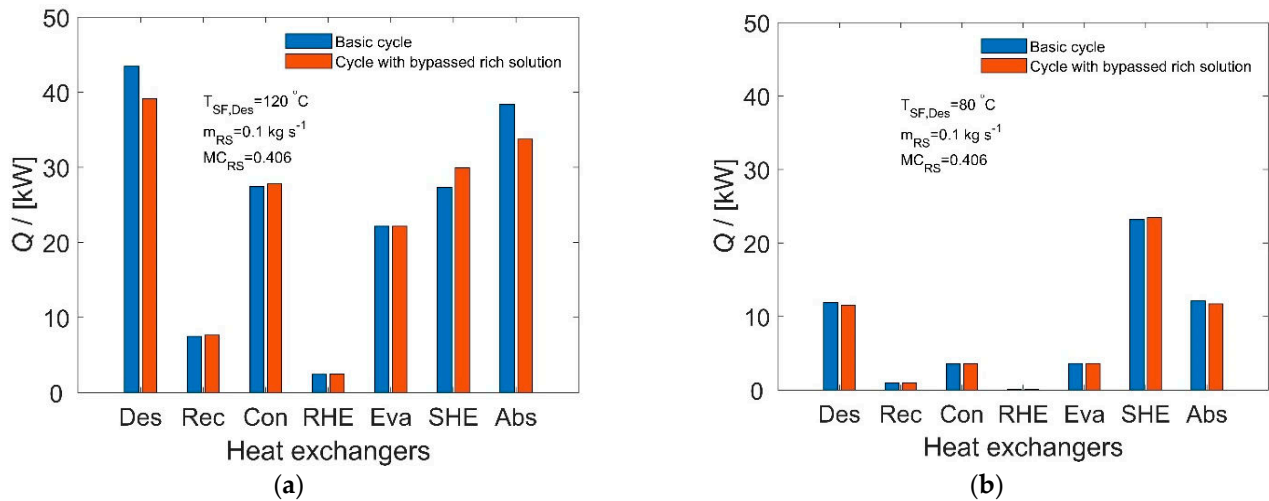


Figure 14. Heat exchanger loads of cycle with bypassed rich solution and basic cycle for different heat source temperature. (a) 120 °C, (b) 80 °C.

The performance of different cycles is compared in Figure 15. Both the cooling capacity and heating capacity of the compression-assisted cycle are increased. More refrigerant is generated. This enhancement had large effects at low heat source temperatures. The cycles with counter-current desorber or bypassed rich solution reduced the heating capacity, while the change of cooling capacity was small. Both cycles had similar effects and were advantageous at high heat source temperatures. The performance improvement of the advanced cycles was dependent on the heat source temperatures.

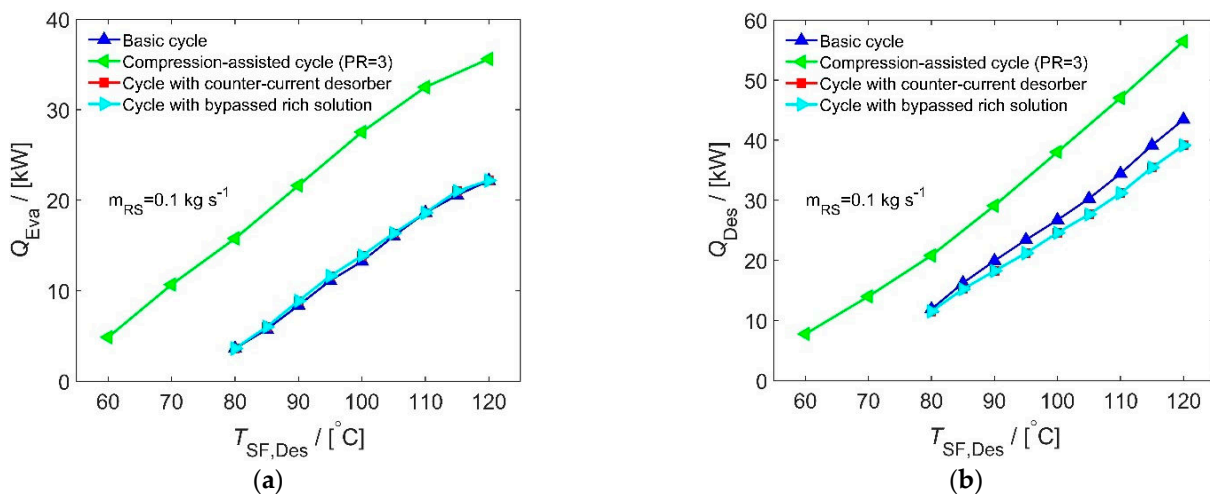


Figure 15. Performance comparison of different cycles. (a) Cooling capacity, (b) Heating capacity.

4.2. Above-Zero Refrigeration

This scenario setted the refrigeration temperature to above zero, and analysed the basic cycle. Table 5 shows the boundary conditions. The hot water temperature increases from 100 °C to 130 °C. The heat sink temperature of the condenser and absorber increases from 25 °C to 35 °C.

Table 5. Input parameters of the heat exchangers and secondary fluids for above-zero refrigeration.

Heat Exchangers	N ^a	A	Secondary Fluid			
			Fluid	T _{in}	P _{in}	m
	-	m ²		°C	kPa	kg s ⁻¹
Des (Type 1)	13/12	1.751	Water	100–130	300	0.8
Con (Type 2)	13/12	0.876	Water	25–35	200	1
Eva (Type 2)	17/16	1.168	Water	20 ^b	200	1
SHE (Type 1)	5/4	0.584	-	-	-	-
Abs (Type 1)	13/12	1.751	Water	25–35	200	0.5

^a Channel number, the secondary fluid/rich solution has one more channel than the working fluid/poor solution.

^b This temperature should be lower if dehumidification is required for the application of air-conditioning.

Compared with sub-zero refrigeration, the rich solution had a higher mass concentration for above-zero refrigeration. Consequently, more refrigerants were generated at the desorber. As shown in Table 5, the condenser and evaporator have larger heat transfer areas.

The heat sink temperature had a major influence on the cycle performance. The mass concentrations of the rich solution were limited by the capacity of the absorber. For higher heat sink temperatures, the mass concentrations were reduced to maintain the temperature driving force. In Figure 16, the influences of heat source temperature and heat sink temperature are analysed. The high and low pressures were determined by trial calculation. The low pressure increased with the heat source temperature for 460–520 kPa so that the working fluid was subcooled at the absorber outlet. The subcooling was 1–29 K. Consequently, the evaporation temperature at the evaporator inlet increased from 3 °C to 6 °C. At the condenser, higher heat sink temperature increased the operating pressures [13]. The temperature driving force was maintained so that the refrigerant was fully condensed. In this analysis, the high pressures were 1250–1550 kPa, 1350–1650 kPa and 1450–1750 kPa for the heat sink temperatures of 25 °C, 30 °C and 35 °C, respectively.

In Figure 16a,b, the cooling capacity and refrigerant mass flow rate decrease with higher heat sink temperature. The rich solution has a lower mass concentration for a higher heat sink temperature, which restrains the generation of refrigerant vapour at the desorber. Additionally, the operating pressure of the desorber is higher for high heat sink temperature. The temperature driving force between the heat source and working fluid is reduced. Higher heat source temperatures increase the cooling capacity and refrigerant mass flow rate. The increase of the refrigerant mass flow rate is almost linear, while the increase of the cooling capacity becomes flat at high heat source temperatures. The reason was that the refrigerant contained more water, which is presented in Figure 16c. The refrigerant mass concentrations decrease with the heat source temperature. The refrigerant leaving the evaporator has a vapour quality of about 0.9 at the heat source of 130 °C. When the heat sink temperature is low, the refrigerant has higher mass concentration.

In Figure 16d, the COP decreases with higher heat sink temperature. Higher heat sink temperature causes the heat transfer of the absorber and condenser to deteriorate. The mass concentrations of the rich solution decrease at the absorber. The operating pressure of the condenser rises. Since the desorber has the same operating pressure as the condenser, less refrigerant is generated. There is a maximum COP. When the heat sink temperature is 35 °C, the maximum COP occurs at a heat source temperature of 115–120 °C. For the heat sink temperature of 25 °C and 30 °C, 110 °C is the optimal heat source temperature.

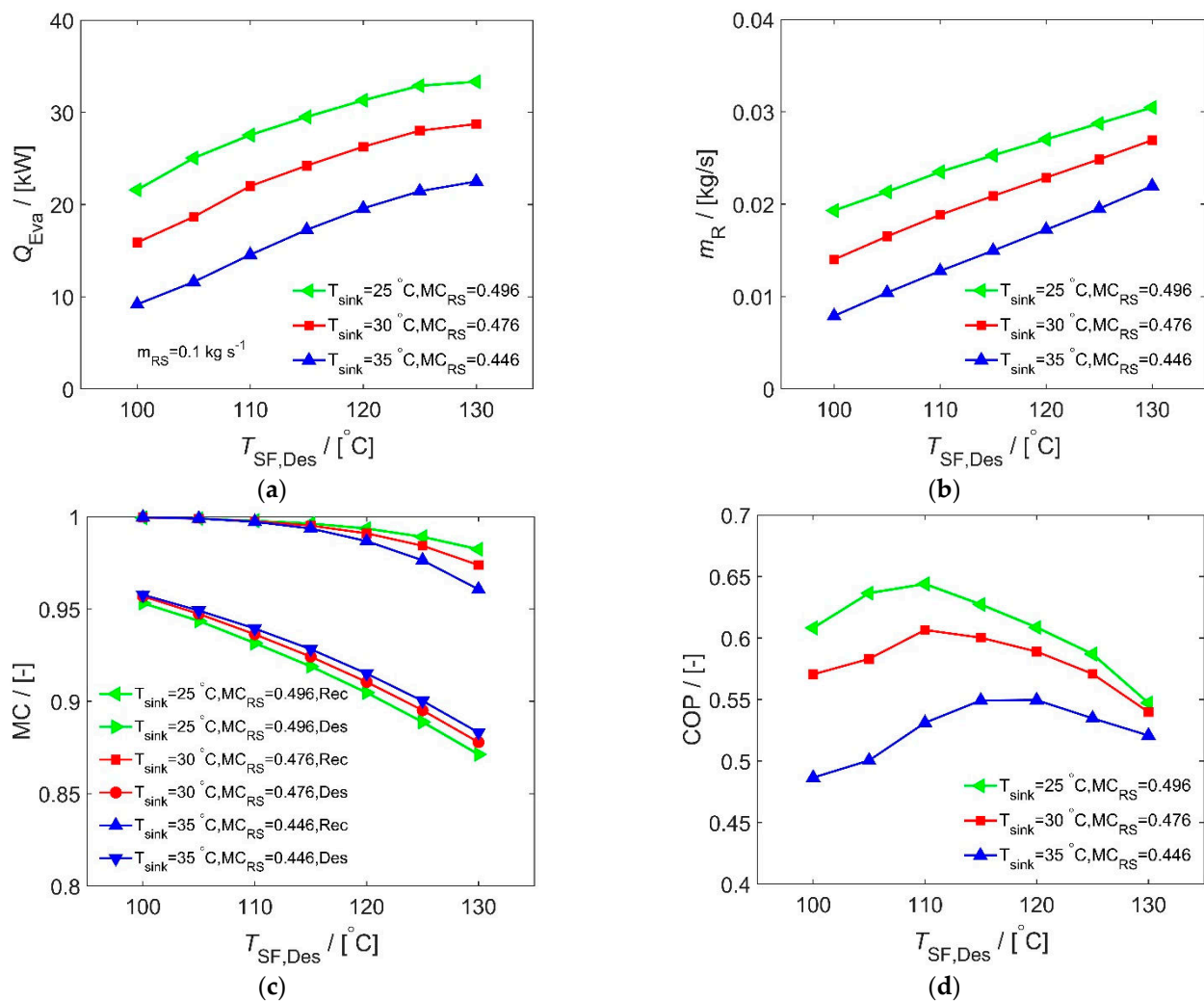


Figure 16. Cycle performances as a function of heat source temperature and heat sink temperature. Cycle performances are (a) Cooling capacity, (b) Refrigerant mass flow rate, (c) Vapour mass concentration at the outlet of the desorber and rectifier, (d) COP.

Figure 17 shows the heat loads of the heat exchangers with different heat sink temperatures. The heat source temperature is 110 °C, achieving a high COP. Higher heat sink temperatures generally reduce the heat loads of the heat exchangers since the refrigerant mass flow rate decreases. The heat loads of the desorber, condenser, evaporator and absorber are mostly latent heat, and are proportional to the refrigerant mass flow rate. The SHE shows different characteristics. When the refrigerant mass flow rate is small, the mass flow rates of the rich solution and poor solution are close, resulting in higher heat exchanger effectiveness. The rectifier has a large heat load so that the vapour is sufficiently purified. The heat loads of the rectifier account for more than 16% of the heating capacity at the desorber. Because of the high refrigerant mass concentration, the evaporator has an equivalent heat load to the condenser. The condensed refrigerant is fully evaporated. The RHE recovers a small amount of cooling capacity.

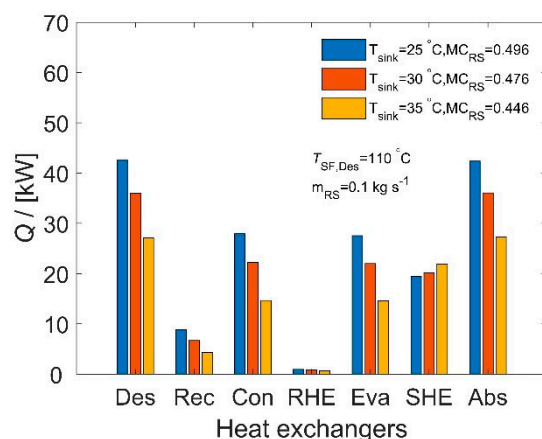


Figure 17. Heat exchanger loads as a function of heat sink temperature.

5. Conclusions

A single-stage ammonia/water absorption chiller was modelled and was validated with experimental data. Sub-zero refrigeration was investigated for the basic cycle and three advanced cycles. Above-zero refrigeration was also analysed for the basic cycle. For all the scenarios, COP initially increased with heat source temperatures but then decreased because of lower refrigerant mass concentrations. The main conclusions are below:

- The COP for the basic cycle of sub-zero refrigeration is 0.23–0.54. The activation temperature of the heat source is 80 °C. The maximum COP is achieved when the heat source temperature is 110 °C. When the heat source temperature is too high, the water content generated at the desorber increases the thermodynamic losses. Higher heat source temperature increases the refrigerant mass flow rate and cooling capacity. The cooling capacity is 2.1–22.4 kW. The rich solution with large mass flow rates and high mass concentration achieves a larger cooling capacity since more refrigerant is generated. The mass flow rates and mass concentrations are restrained by the heat transfer performance of the absorber.
- The compression-assisted cycle reduces the activation temperature of the heat source. Compared with the basic cycle, this cycle produces more refrigerant and cooling capacity, especially at low heat source temperatures. The cooling capacity is increased by around 12 kW at the pressure ratio of 3. The COP increases to 0.47–0.65 at the cost of more compressor power consumption.
- The cycle with counter-current desorber increases the mass concentration of outlet vapour and reduces the heating capacity. The COP is 0.31–0.58, and is improved by about 7% relative to the basic cycle. The cycle with bypassed rich solution optimises the internal heat recovery of the SHE. The COP is 0.31–0.59. The counter-current desorber and bypassed rich solution improve their performance significantly at high heat source temperatures.
- The COP for above-zero refrigeration is 0.48–0.65. The optimal heat source temperature for COP depends on the heat sink temperatures. A higher heat source temperature is needed with a high heat sink temperature. A higher heat source temperature and a lower heat sink temperature increase the cooling capacity. The maximum cooling capacity is 33.3 kW.

Author Contributions: Conceptualization, X.T. and K.P.; methodology, X.T.; validation, X.T.; formal analysis, X.T.; investigation, X.T., D.T. and K.P.; resources, K.P.; data curation, X.T.; writing—original draft preparation, X.T.; writing—review and editing, D.T. and K.P.; visualisation, X.T. and D.T.; supervision, K.P.; project administration, K.P.; funding acquisition, K.P. All authors have read and agreed to the published version of the manuscript.

Funding: This work was funded by the British Council Newton Institutional Links project under low grade heat recovery for absorption chiller and desalination from concentrated solar-powered steam power plants in Egypt, and the Innovate UK funded project (78689) on Development of a low carbon heating and cooling system with storage and gender based temperature regulation for public and commercial buildings.

Data Availability Statement: Data available within the article. The authors confirm that the data supporting the findings of this study are available within the article.

Acknowledgments: Carlos Infante Ferreira from TU Delft shared his experience about the design and operation of absorption systems. Peter Turner provided constructive feedback on the paper. During the International Sorption Heat Pump Conference 2021 held by TU Berlin, the author had fruitful discussions with the participants. Their comments are highly appreciated. Neng Gao from Ningbo Institute of Technology provided helpful advice on fluid properties.

Conflicts of Interest: The authors declare no conflict of interest.

Nomenclature

Symbols

A	Actual heat transfer area [m ²]
Bo	Boiling number [-]
Co	Convection number [-]
COP	Coefficient of performance [-]
c_p	Specific heat [Jkg ⁻¹ K ⁻¹]
d_g	Channel gap [mm]
d_h	Hydraulic diameter [m]
d_p	Plate thickness [mm]
f	Solution circulation ratio [-]
f_D	Darcy friction factor [-]
Fr	Froude number [-]
g	Gravitational constant [ms ⁻²]
h	Enthalpy [kJkg ⁻¹]
$LMTD$	Log mean temperature difference [K]
L_p	Effective plate length [mm]
m	Mass flow rate [kgs ⁻¹]
MC	Mass concentration [-]
P	Pressure [kPa]
Pr	Prandtl number [-]
Q	Heat transfer rate [kW]
Re	Reynolds number [-]
T	Temperature [°C]
U	Overall heat transfer coefficient [Wm ⁻² K ⁻¹]
u	Superficial velocity [ms ⁻¹]
W	Power [kW]
We	Weber number [-]
W_p	Effective plate width [mm]
x	Vapour quality [-]
Greek symbols	
α	Heat transfer coefficient [Wm ⁻² K ⁻¹]
β	Chevron angle to flow direction [°]
Δ	Difference [-]
Φ	Surface enlargement factor [-]
$\phi_{Chisholm}$	Two-phase friction multiplier [-]
λ	Thermal conductivity [Wm ⁻¹ K ⁻¹]
Λ_{wave}	Corrugation wavelength [mm]
μ	Dynamic viscosity [Pas]
ρ	Density [kgm ⁻³]

Subscripts	
C	Cooling water
Cold	Cold fluid
Cri	At critical conditions
eq	Equivalent
high	High pressure side
hot	Hot fluid
in	Inlet
L	Liquid
LO	Liquid only
low	Low pressure side
LTi	Limits in Equations (A2)-(A3)
LV	Latent liquid to vapor
out	Outlet
PS	Poor solution
R	Refrigerant
RS	Rich solution
sat	At saturation conditions
sink	Heat sink
source	Heat source
SF	Secondary fluid
TP	Two-phase
V	Vapour
wall	At wall conditions
WF	Working fluid
Abbreviations	
Abs	Absorber or absorption process
Com	Compressor
Con	Condenser or condensation process
Des	Desorber or desorption process
Eva	Evaporator or evaporation process
Exp	Experimental data
HTC	Heat transfer coefficient
Per	For each heat exchanger plate
PHE	Plate heat exchanger
PR	Pressure ratio
Pre	Predicted data
Rec	Rectifier
RHE	Refrigerant heat exchanger
SHE	Solution heat exchanger
SP	Solution pump

Appendix A

PHEs are used as the desorber, condenser, evaporator, absorber and SHEs. The heat transfer and pressure drop correlations are described below. The definitions of non-dimensional numbers are listed in Tao and Infante Ferreira [47].

The liquid heat transfer coefficient is given in Equation (A1), which is used to predict the working fluid of solution heat exchanger and the secondary fluids of other heat exchangers [40]. It is a function of Darcy friction factor, f_D , and the chevron angle of plate heat exchanger, β . f_D is calculated using Equations (A2)–(A4). Equation (A1) is also used to predict the liquid-only heat transfer coefficient included in the two-phase heat transfer, which is shown in Equations (A5) and (A8). The pressure drops of the secondary fluids are calculated with Equations (A2)–(A4).

$$\alpha_L = 0.122(f_D \sin 2\beta)^{0.374} Re_L^{0.748} Pr_L^{0.333} \left(\frac{\mu}{\mu_{wall}} \right)^{0.167} \frac{\lambda_L}{d_h} \quad (A1)$$

$$f_{D,LT1} = \begin{cases} 64Re^{-1}, & Re < 2000 \\ (1.8 \log_{10}(Re) - 1.5)^{-2}, & Re \geq 2000 \end{cases} \quad (A2)$$

$$f_{D,LT2} = \begin{cases} 3.8(597Re^{-1} + 3.85), & Re < 2000 \\ 3.8(39Re^{-0.289}), & Re \geq 2000 \end{cases} \quad (A3)$$

$$f_D = \left(\frac{\cos \beta}{\sqrt{0.18 \tan \beta + 0.36 \sin \beta + f_{D,LT1} / \cos \beta}} + \frac{1 - \cos \beta}{\sqrt{f_{D,LT2}}} \right)^{-2} \quad (A4)$$

The desorption correlation of Taboas et al. [33] is shown in Equation (A5). u_V and u_L are the superficial velocities of vapour and liquid, respectively. Bo is boiling number. α_{LO} is liquid-only heat transfer coefficient. $\phi_{Chisholm}$ is two-phase friction multiplier. This correlation combines nucleate boiling and convective boiling. The dominant boiling mechanism depends on the superficial velocities of vapour and liquid. This correlation is derived from experimental data and is applicable for the mass fluxes of 50–150 kg m⁻² s⁻¹ and the vapour qualities of 0–0.2 [34]. The mass concentrations are 0.42–0.62. The operating pressures are 700–1500 kPa. The heat fluxes are 20–50 kW m⁻².

$$\begin{cases} \alpha_{Des} = 5Bo^{0.15} \alpha_{LO}, & u_V < -111.88u_L + 11.848 \\ \alpha_{Des} = \max \left\{ 5Bo^{0.15} \alpha_{LO}, (\phi_{Chisholm}^2)^{0.2} \alpha_{LO} \right\}, & u_V > -111.88u_L + 11.848 \end{cases} \quad (A5)$$

Equation (A6) is the correlation of absorption in bubble mode [35]. Re_L , Re_C and Re_V are the liquid Reynolds number, cooling water Reynolds number and vapor Reynolds number, respectively. ΔP is the pressure drop.

$$\begin{aligned} \alpha_{Abs} &= 691.60Re_L^{0.36}Re_C^{-0.80}Re_V^{0.10}Pr_L^{-0.41}\Delta P^{-0.19}\frac{\lambda_L}{d_h} \\ Re_L &= 213 - 572, Re_C = 280 - 590, Re_V = 759 - 1994 \end{aligned} \quad (A6)$$

The evaporation of ammonia is predicted using Equation (A7) [37]. Re_{eq} and Bo_{eq} are equivalent Reynolds number and equivalent Boiling number, respectively. This correlation is applicable for the operating conditions that the inlet is subcooled liquid and the outlet is two-phase with the vapour qualities of 0.5–0.9. The saturation temperature is –25 °C to –2 °C. The heat fluxes are 21–44 kW m⁻².

$$\begin{aligned} \alpha_{Eva} &= 82.5(Re_{eq}Bo_{eq})^{-0.085} \left(\frac{P_{sat}}{P_{cri}} \right)^{0.21} \frac{\lambda_L}{d_h} \\ Re_{eq} &= 1387 - 2200 \end{aligned} \quad (A7)$$

Ammonia condensation is calculated with Equation (A8) [36]. We_L is the liquid Weber number. Co and Fr_L are the convection number and liquid Froude number. This correlation applies to the vapor qualities of 0–0.8 and the mass fluxes of 20–80 kgm⁻²s⁻¹. This correlation was originally developed for the saturation pressure below 1000 kPa and can be extended to higher pressure since the fluid properties of ammonia change slightly with operating pressure.

$$\begin{cases} \alpha_{Con} = \alpha_{LO} \left(0.17Co^{-1.12}Fr_L^{-0.2} + (1-x)^{0.748} \right), & We_L \geq 0.12 \\ \alpha_{Con} = \alpha_{LO} \left(0.17Co^{-1.12}Fr_L^{-0.2} + (1-x)^{0.748} \right) \frac{We_L}{0.12} + \\ 0.36Co^{-0.28} \left(\frac{g\rho_L(\rho_L - \rho_V)\Delta h_{LV}\lambda_L^3}{\mu_L\Delta T d_h} \right)^{0.25} Pr_L^{0.333} \frac{0.12 - We_L}{0.12}, & We_L < 0.12 \end{cases} \quad (A8)$$

The condensation heat transfer of high concentration ammonia/water degrades compared with pure ammonia. The reduction of HTC is calculated with the Silver [38] and Bell and Ghaly [39] method, which is given in Equation (A9). The mass transfer resis-

tance is proportional to the heat transfer resistance of the vapor, α_V^{-1} , and derivative of temperature with enthalpy, dT/dh .

$$\alpha_{ammonia/water} = \left(\alpha_{ammonia}^{-1} + x c_{p,V} \frac{dT}{dh} \alpha_V^{-1} \right)^{-1} \quad (A9)$$

The working fluid is two-phase flow during desorption, condensation, evaporation and absorption. The relevant pressure drops are calculated using Equation (A10) [36]. This correlation was originally developed for pure ammonia, and applies to the vapor qualities of 0–1 and the mass fluxes of 20–80 $\text{kgm}^{-2}\text{s}^{-1}$. It is also applicable for ammonia/water [28]. The two-phase pressure drop is the sum of liquid pressure drop, vapor pressure drop and interface pressure drop. The single-phase pressure drop is predicted with Equations (A2)–(A4).

$$\Delta P_{TP} = \Delta P_L + 2\sqrt{\Delta P_L \Delta P_V} + x \Delta P_V \quad (A10)$$

References

1. IEA. *The Future of Cooling: Opportunities for Energy-Efficient Air Conditioning*; IEA: Paris, France, 2018.
2. Kim, D.S.; Infante Ferreira, C.A. Solar refrigeration options—a state-of-the-art review. *Int. J. Refrig.* **2008**, *31*, 3–15.
3. Garciadealva, Y.; Best, R.; Gómez, V.H.; Vargas, A.; Rivera, W.; Jiménez-García, J.C. A Cascade Proportional Integral Derivative Control for a Plate-Heat-Exchanger-Based Solar Absorption Cooling System. *Energies* **2021**, *14*, 4058. [CrossRef]
4. Kalogirou, S.A. *Solar Energy Engineering: Processes and Systems*; Academic Press: Cambridge, MA, USA, 2009.
5. Herold, K.E.; Radermacher, R.; Klein, S.A. *Absorption Chillers and Heat Pumps*; CRC Press: Boca Raton, FL, USA, 2016.
6. Siddiqui, M.U.; Said, S.A.M. A review of solar powered absorption systems. *Renew. Sustain. Energy Rev.* **2015**, *42*, 93–115.
7. Lima, A.A.S.; Leite, G.d.N.P.; Ochoa, A.A.V.; Santos, C.A.C.d.; Costa, J.A.P.d.; Michima, P.S.A.; Caldas, A.M.A. Absorption Refrigeration Systems Based on Ammonia as Refrigerant Using Different Absorbents: Review and Applications. *Energies* **2021**, *14*, 48. [CrossRef]
8. Altamirano, A.; Le Pierrès, N.; Stutz, B. Review of small-capacity single-stage continuous absorption systems operating on binary working fluids for cooling: Theoretical, experimental and commercial cycles. *Int. J. Refrig.* **2019**, *106*, 350–373.
9. Abed, A.M.; Alghoul, M.A.; Sopian, K.; Majidi, H.S.; Al-Shamani, A.N.; Muftah, A.F. Enhancement aspects of single stage absorption cooling cycle: A detailed review. *Renew. Sustain. Energy Rev.* **2017**, *77*, 1010–1045.
10. Kang, Y.T.; Kunugi, Y.; Kashiwagi, T. Review of advanced absorption cycles: Performance improvement and temperature lift enhancement. *Int. J. Refrig.* **2000**, *23*, 388–401.
11. Chen, X.; Wang, R.Z.; Du, S. An improved cycle for large temperature lifts application in water-ammonia absorption system. *Energy* **2017**, *118*, 1361–1369.
12. Du, S.; Wang, R.Z.; Xia, Z.Z. Optimal ammonia water absorption refrigeration cycle with maximum internal heat recovery derived from pinch technology. *Energy* **2014**, *68*, 862–869. [CrossRef]
13. Goyal, A.; Staedter, M.A.; Hoysall, D.C.; Ponkala, M.J.; Garimella, S. Experimental evaluation of a small-capacity, waste-heat driven ammonia-water absorption chiller. *Int. J. Refrig.* **2017**, *79*, 89–100.
14. Staedter, M.A.; Garimella, S. Development of a micro-scale heat exchanger based, residential capacity ammonia–water absorption chiller. *Int. J. Refrig.* **2018**, *89*, 93–103.
15. Delahanty, J.C.; Hughes, M.; Garimella, S. Desorber and Rectifier Geometries for Ammonia-Water Absorption Systems; Part I: Experimental Approach and Heat Transfer. *Int. J. Refrig.* **2021**, *123*, 111–123.
16. Staedter, M.A.; Garimella, S. Design and modeling of a microscale diabatic distillation column for small capacity ammonia–water absorption systems. *Int. J. Refrig.* **2018**, *94*, 161–173.
17. Wu, W.; Shi, W.; Wang, J.; Wang, B.; Li, X. Experimental investigation on NH₃–H₂O compression-assisted absorption heat pump (CAHP) for low temperature heating under lower driving sources. *Appl. Energy* **2016**, *176*, 258–271. [CrossRef]
18. Wu, W.; Wang, B.; Shang, S.; Shi, W.; Li, X. Experimental investigation on NH₃–H₂O compression-assisted absorption heat pump (CAHP) for low temperature heating in colder conditions. *Int. J. Refrig.* **2016**, *67*, 109–124.
19. Le Lostec, B.; Galanis, N.; Millette, J. Experimental study of an ammonia-water absorption chiller. *Int. J. Refrig.* **2012**, *35*, 2275–2286.
20. Jiménez-García, J.C.; Rivera, W. Parametric analysis on the experimental performance of an ammonia/water absorption cooling system built with plate heat exchangers. *Appl. Therm. Eng.* **2019**, *148*, 87–95.
21. Chen, X.; Wang, R.Z.; Du, S. Heat integration of ammonia-water absorption refrigeration system through heat-exchanger network analysis. *Energy* **2017**, *141*, 1585–1599.
22. Lin, P.; Wang, R.Z.; Xia, Z.Z. Numerical investigation of a two-stage air-cooled absorption refrigeration system for solar cooling: Cycle analysis and absorption cooling performances. *Renew. Energy* **2011**, *36*, 1401–1412.

23. Said, S.A.M.; El-Shaarawi, M.A.I.; Siddiqui, M.U. Analysis of a solar powered absorption system. *Energy Convers. Manag.* **2015**, *97*, 243–252.
24. Bogart, M.J.P. Pitfalls in ammonia absorption refrigeration. *Int. J. Refrig.* **1982**, *5*, 203–208.
25. Wageiallah Mohammed, O.; Yanling, G. Comprehensive Parametric Study of a Solar Absorption Refrigeration System to Lower Its Cut In/Off Temperature. *Energies* **2017**, *10*, 1746. [CrossRef]
26. Fernández-Seara, J.; Sieres, J.; Vázquez, M. Distillation column configurations in ammonia–water absorption refrigeration systems. *Int. J. Refrig.* **2003**, *26*, 28–34. [CrossRef]
27. Fernández-Seara, J.; Sieres, J. The importance of the ammonia purification process in ammonia–water absorption systems. *Energy Convers. Manag.* **2006**, *47*, 1975–1987.
28. Tao, X.; Infante Ferreira, C. Absorption of high concentration NH₃/H₂O in a plate heat exchanger. In Proceedings of the ISHPC 2021 Proceedings, Berlin/Heidelberg, Germany, 22–25 August 2021; Volume 108.
29. Mathworks. Matlab R2019a. 2019. Available online: <https://www.mathworks.com/help/matlab/> (accessed on 5 April 2021).
30. Staedter, M.A.; Garimella, S. Heat and mass transfer in microscale diabatic distillation columns for ammonia–water desorption and rectification. *Int. J. Refrig.* **2018**, *95*, 10–20.
31. Stoffel, B. Chapter 4—Physical and Technical Background of the Efficiency of Pumps. In *Assessing the Energy Efficiency of Pumps and Pump Units*; Stoffel, B., Ed.; Elsevier: Boston, MA, USA, 2015; pp. 45–61. [CrossRef]
32. Tao, X.; Nuijten, M.P.; Infante Ferreira, C.A. Two-phase vertical downward flow in plate heat exchangers: Flow patterns and condensation mechanisms. *Int. J. Refrig.* **2018**, *85*, 489–510. [CrossRef]
33. Taboas, F.; Valles, M.; Bourouis, M.; Coronas, A. Assessment of boiling heat transfer and pressure drop correlations of ammonia/water mixture in a plate heat exchanger. *Int. J. Refrig.* **2012**, *35*, 633–644.
34. Táboas, F.; Vallès, M.; Bourouis, M.; Coronas, A. Flow boiling heat transfer of ammonia/water mixture in a plate heat exchanger. *Int. J. Refrig.* **2010**, *33*, 695–705.
35. Cerezo, J.; Best, R.; Bourouis, M.; Coronas, A. Comparison of numerical and experimental performance criteria of an ammonia–water bubble absorber using plate heat exchangers. *Int. J. Heat Mass Transf.* **2010**, *53*, 3379–3386.
36. Tao, X.; Infante Ferreira, C.A. NH₃ condensation in a plate heat exchanger: Flow pattern based models of heat transfer and frictional pressure drop. *Int. J. Heat Mass Transf.* **2020**, *154*, 119774. [CrossRef]
37. Khan, T.S.; Khan, M.S.; Chyu, M.-C.; Ayub, Z.H. Experimental investigation of evaporation heat transfer and pressure drop of ammonia in a 60 chevron plate heat exchanger. *Int. J. Refrig.* **2012**, *35*, 336–348. [CrossRef]
38. Silver, L. Gas cooling with aqueous condensation. *Trans. Inst. Chem. Eng* **1947**, *25*, 30–42.
39. Bell, K.J.; Ghaly, M.A. An approximate generalized design method for multicomponent/partial condenser. *AIChE Symp. Ser.* **1972**, *69*, 72–79.
40. Martin, H. A theoretical approach to predict the performance of chevron-type plate heat exchangers. *Chem. Eng. Process. Process Intensif.* **1996**, *35*, 301–310. [CrossRef]
41. Tao, X.; Dahlgren, E.; Leichsenring, M.; Infante Ferreira, C.A. NH₃ condensation in a plate heat exchanger: Experimental investigation on flow patterns, heat transfer and frictional pressure drop. *Int. J. Heat Mass Transf.* **2020**, *151*, 119374. [CrossRef]
42. Lemmon, E.W.; Bell, I.H.; Huber, M.L.; McLinden, M.O. *NIST Standard Reference Database 23, Reference Fluid Thermodynamic and Transport Properties (REFPROP), Version 10.0*; National Institute of Standards and Technology: Gaithersburg, MD, USA, 2018. Available online: <http://www.nist.gov/srd/nist23.cfm> (accessed on 1 May 2021).
43. Conde, M. *Thermophysical Properties of NH₃ + H₂O Solutions for the Industrial Design of Absorption Refrigeration Equipment*; M. Conde Engineering: Zurich, Switzerland, 2004.
44. Melinder, Å. *Thermophysical Properties of Aqueous Solutions Used as Secondary Working Fluids*; KTH: Stockholm, Sweden, 2007.
45. Albers, J.; Ziegler, F. Analysis of the part load behaviour of sorption chillers with thermally driven solution pumps. In Proceedings of the 21th IIR International Congress of Refrigeration, Washington DC, USA, 17–22 August 2003.
46. Gudjonsdottir, V.; Infante Ferreira, C.A.; Goethals, A. Wet compression model for entropy production minimization. *Appl. Therm. Eng.* **2019**, *149*, 439–447. [CrossRef]
47. Tao, X.; Infante Ferreira, C.A. Heat transfer and frictional pressure drop during condensation in plate heat exchangers: Assessment of correlations and a new method. *Int. J. Heat Mass Transf.* **2019**, *135*, 996–1012. [CrossRef]